Science of the Total Environment 822 (2022) 153661

Contents lists available at ScienceDirect

Science of the Total Environment

journal homepage: www.elsevier.com/locate/scitotenv

Flood characterization based on forensic analysis of bridge collapse using UAV reconnaissance and CFD simulations

Marianna Loli [a,*], Stergios Aristoteles Mitoulis [a,1], Angelos Tsatsis [b], John Manousakis [c], Rallis Kourkoulis [b], Dimitrios Zekkos [d]

[a] University of Surrey, Department of Civil and Environmental Engineering, UK
[b] Grid Engineers, Greece
[c] Elxis Group, Athens, Greece
[d] Department of Civil and Environmental Engineering, University of California, Berkeley, CA, United States

HIGHLIGHTS

- Extreme weather event
- Failure
- Flooding
- Numerical modelling
- UAV survey

GRAPHICAL ABSTRACT

Fig. A novel approach for a posteriori assessment of the intensity of an extreme flood event.

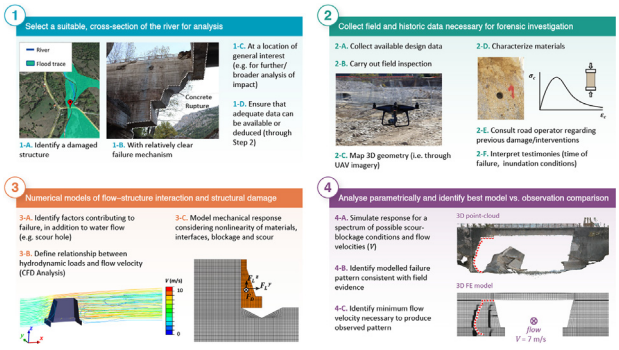

ARTICLE INFO

Article history:
Received 24 September 2021
Received in revised form 23 December 2021
Accepted 30 January 2022
Available online 3 February 2022

Editor: Martin Drews

Keywords:
Extreme weather event
Flash flood
Bridge Failure
Case study
Forensic Investigation
UAV surveying
Numerical modelling

ABSTRACT

Flash floods are common manifestations of extreme weather events and one of the most severe natural hazards. In Europe, they have been responsible for 359 fatalities and an economic loss totalling 67 million USD in the past decade (EM-DAT), while their increasing severity is linked to climate change. Nevertheless, flash floods remain a poorly documented natural phenomenon due to the lack of flow intensity data in many of the affected watersheds. Based on a thorough field investigation, including UAV-based 3D mapping and material characterization with on-site testing, we carry out a numerical study of a notable flood that caused the collapse of bridges and buildings in Central Greece, following a recent Mediterranean hurricane. Focusing on a carefully selected case study, we combine 3D modelling of flow–structure interaction with detailed mechanical modelling of the nonlinear structural response to reproduce the flood-induced fracture of a bridge abutment. Back-analysis of this failure responds to the fundamental problem of estimating the undocumented magnitude of this extreme event. The paper estimates a lower bound value of the flow velocity at the studied location. This can be valuable input for the interpretation of the extensive damage that took place downstream and for the re-assessment of flood risk in a region where similar events are expected to become more frequent because of climate change. The approach, where disaster forensics and engineering analysis are used to fill the gap of missing real-time measurements, can be implemented for the a posteriori estimation of flood

* Corresponding author.
E-mail address: m.loli@surrey.ac.uk (M. Loli).
[1] infrastructuResilience: http://www.infrastructuresilience.com/.

http://dx.doi.org/10.1016/j.scitotenv.2022.153661

UAV mapping
Scour
Riverbank erosion
Abutment vulnerability

intensity in similar events. The well-documented case study of a bridge failure due to extreme flooding can also be used for validation of future numerical and experimental methods and motivate investigations of the mechanisms governing flow–soil–structure interaction in river crossings.

1. Introduction

Urbanization and the increasing degree of interdependence between economic activities are sufficient conditions to cause rising trends in flood risk (Kundzewicz et al., 2014; Zischg et al., 2018), let alone climate change (Kendon et al., 2014). Probabilistic analysis of extreme river discharges in Europe (Jongman et al., 2014) indicates that catastrophic events are likely to become twice as frequent and costly, by 2050. The vast scale of destruction caused by major floods that impacted the western part of Europe in July 2021, only weeks before the submission of this paper, has stressed in the most emphatic way the severity of this prediction. Over 180 fatalities and hundreds of thousands of damaged households, amid the widespread failure of communication networks and lifelines, are only a first account of the toll paid mostly by Germany, Belgium, and the Netherlands (Cornwall, 2021) — a region where investment in early warning and flood protection has been relatively high in comparison to other parts of the world.

Flash floods are characterized by short warnings and high discharges, a combination that amounts to one of the most severe and catastrophic natural hazards with widespread ramifications. Despite growing research interest in the characterization of flash floods and efforts to create comprehensive databases of past events (Gaume et al., 2009; Marchi et al., 2010; Llasat et al., 2010), they remain poorly documented. As flash floods often affect ungauged watersheds, discharge information and data on their hydraulic characteristics is scarce, affecting our ability to accurately assess risk and resilience. This gap in our understanding of flash flood intensity is, admittedly, one of the missing pieces in the "jigsaw" (CEH, 1999) that we have to solve to enable improved hazard assessment, warning, and emergency management. What is more, climate adaptation of our critical infrastructure and their ecosystems is far from being tangible without accurate data on the intensity of flash floods.

The primary objective of the forensic investigation presented in this paper is to provide quantifiable evidence on the intensity of a major flooding event that severely impacted Greece in September 2020, following the passage of the Mediterranean hurricane (Medicane) Ianos. A 4-step approach for a posteriori assessment of flood intensity has been developed and is summarized in Fig. 1. It integrates field data (Step 2) to create high-fidelity numerical models (Step 3) that capture the sensitivity of the simulated damage pattern to the details of loading and the intensity of the flow. Thereby, the method can distinguish the most probable, among the investigated loading scenarios, based on the similarity between modelled and observed responses (Step 4). It relies on the selection of a representative, suitable cross-section of the flooded channel, where a significantly damaged structure is located (Step 1). The output is an estimate of flow velocity (a typical measure of flood intensity) and therefore the method is effective in cases where hydrodynamic loads acting on the structure are significant in magnitude (as in flash floods). The method provides a local estimate of flood intensity. Nevertheless, this can be a useful point for hydraulic simulations of flood propagation.

In this study, forensic investigations were conducted in conjunction with UAV surveying and in-situ structural material characterization (Step 2). The reference location is the site of an eye-catching bridge failure that took place along river Pamissos. It was selected for its proximity to the town of Mouzaki (Central Greece), which was the hot spot of the event, and for its characteristic failure mechanism, as detailed in the following. Given the lack of discharge measurements in the area, our results contribute to the ongoing discussion about the magnitude of one of the most destructive floods that have affected the country. This becomes particularly

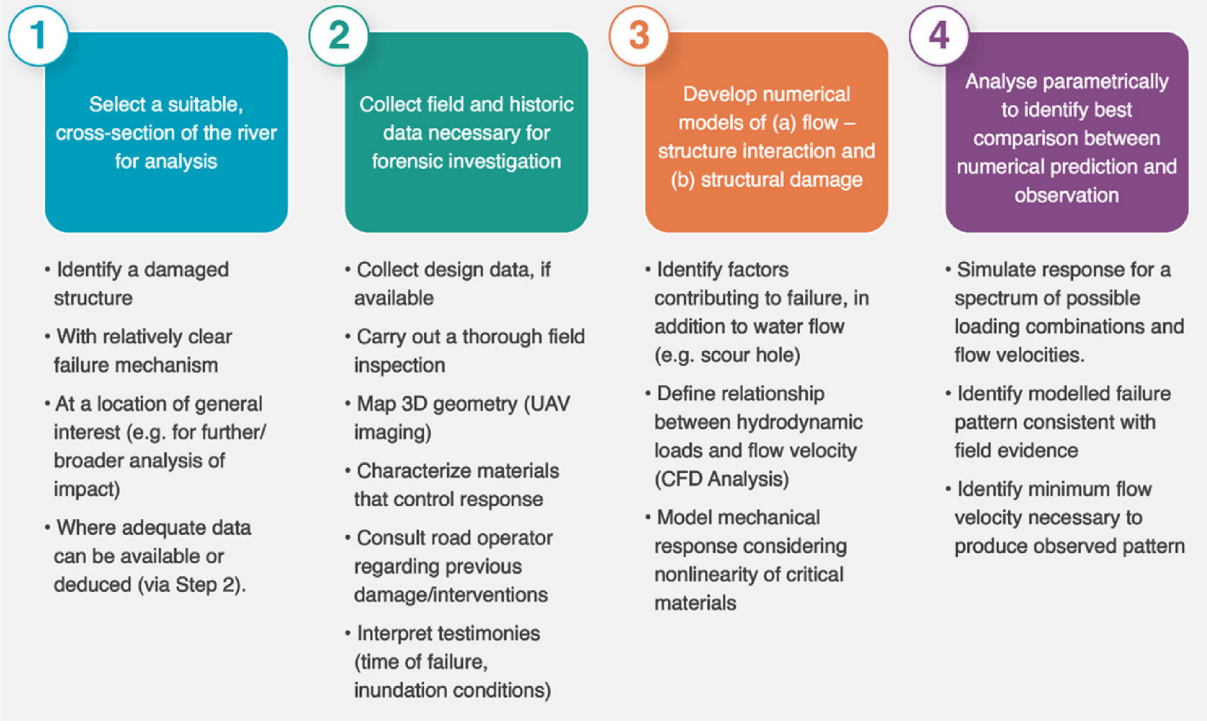

Fig. 1. A posteriori assessment of flood intensity: Method used to back-calculate flow velocity with respect to observed damage.

important given the growing concerns over the potential impact of global warming on medicane activity. Recent high-resolution climate models (Tous et al., 2016; González-Alemán et al., 2019) suggest that medicanes are likely to rise in intensity by the end of the 21st century. A shift towards more tropical weather systems is expected to be accompanied by projections of more intense precipitation and an increased likelihood of future medicanes escalating to hurricane intensity. What is more, a change in the usual cyclone genesis location and path is predicted, with medicanes becoming more common in the eastern Mediterranean (Ionian Sea, Greece). This paper is one of the first to analyse the impact of such an event in the region, where societies and infrastructure operators are unaccustomed to the associated hazards. Additionally, provided insights on the critical role of flow blockage and scour in bridge performance can enhance understanding of the vulnerability of river crossings and associated transportation networks.

Bridges often fail during major floods, yet the parameters that control their failure, namely the exact geometry, the materials, design characteristics, the loading conditions, etc., seldom become available to the level of detail necessary to allow reproduction of the response numerically or experimentally. Thanks to a rapid damage reconnaissance, enabled by use of UAVs, and material field testing conducted soon after the event, before the onset of restoration works, this paper presents the case study in a comprehensive manner that allows its use as reference for validation and further investigation by future research studies.

1.1. Background information: medicane Ianos

Medicanes are intense storms that form over the Mediterranean Sea. Resembling tropical cyclones, they develop a warm core, symmetric structure and concentric convective clouds around a central eye-like feature. On 17 September 2020, the "Ianos" medicane struck Greece (Fig. 2a) causing heavy precipitation that exceeded in various locations the mean annual precipitation. Ianos was an extreme weather event in terms of intensity and duration (17–19 September 2020) classified as one of the most powerful Mediterranean Cyclones recorded since 1969 (Zekkos and Zalachoris, 2020), i.e., since the beginning of satellite observations. It affected a relatively wide area, extending from the Ionian islands, in the west, to the eastern coast of the mainland. The maximum daily accumulated values, as measured by the network of automatic meteorological stations of the National Observatory of Athens, reached up to 317 mm (peak recorded in Pertouli, northwest of Karditsa) and were among the highest recorded in Greece during the past decade.

The severity and spread of destruction were unprecedented. In the mountainous regions, the catastrophic consequences of flash flooding included numerous landslides, debris flows, and erosion, impacting buildings, transportation infrastructure, and powerlines. In the low-lying areas of the Thessaly Plain, large scale flooding with the inundation of over 400 km^2 of agricultural and urban land (Zekkos and Zalachoris, 2020), caused widespread disruptions to communities and severe impact on the economic

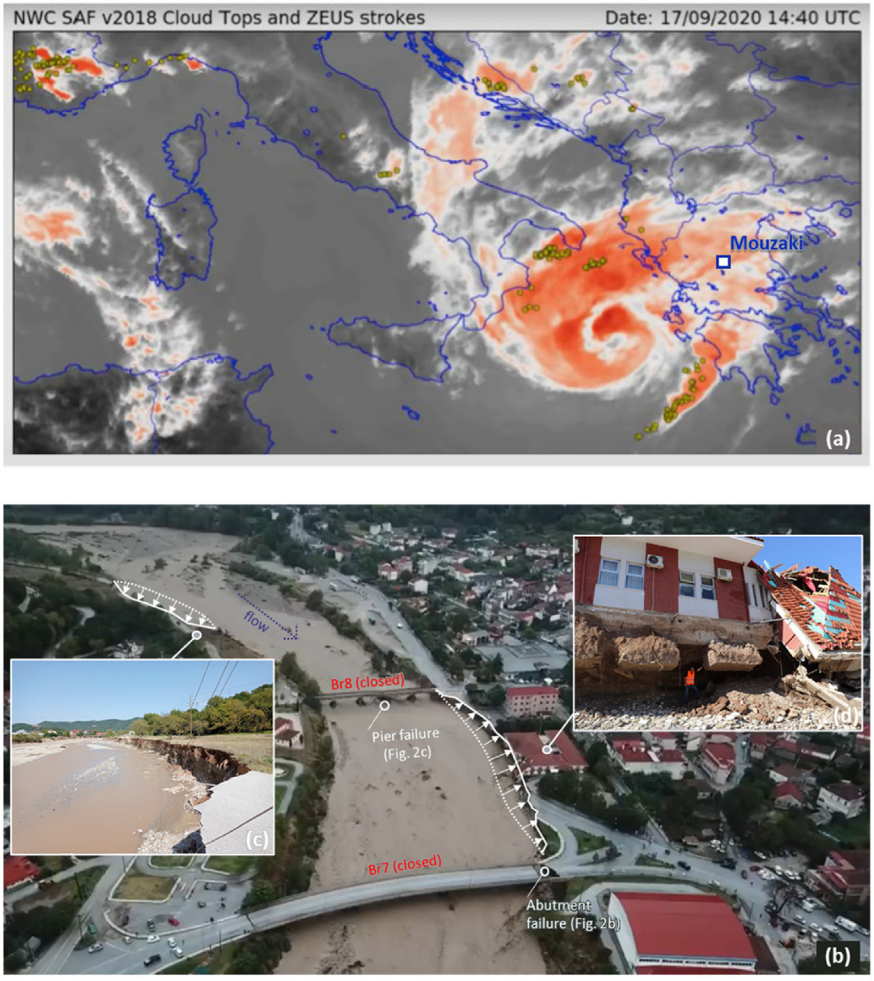

Fig. 2. Impact of the medicane: (a) satellite image of Ianos from METEOSAT-11 on 17/09/20 at 14.40 UTC (Zekkos and Zalachoris, 2020); (b) drone footage captured on September 19, 2020 (by local media) showing the extent of damage in the town of Mouzaki and photos of select failures caused by riverbank erosion: (c) roadway washout; and (d) collapsed hospital.

activity, especially in the city of Karditsa. Four of the authors of this paper participated in a field reconnaissance of the affected areas mobilized by the US GEER Association in October 2020. The relevant report (Zekkos and Zalachoris, 2020) provided a preliminary, broad assessment of the medicane impact, based on a systematic collection of field observations and forensic engineering evidence.

Fig. 2b shows the dramatic condition in which the town of Mouzaki was found one day after the end of the storm. Flash flooding and overflowing of Pamissos river led to widespread devastation including erosion of its gabion-protected riverbanks, sweeping away roadways (Fig. 2c), cars (causing one fatality), and electricity poles. The area was left without power soon after the onset of the storm while its only hospital collapsed due to scour of its foundations, albeit with no fatalities as it was timely evacuated (Fig. 2d).

All five bridges that exist in the area, within a radius of 3 km from the town's centre, suffered extensive damage or complete failure, resulting in a widespread loss of serviceability of the local transportation network. Following the labelling of reported damages adopted by Zekkos and Zalachoris (2020), Fig. 3 shows the location of the bridges in addition to the trace of flooding along Pamissos river, as estimated by the E.U. Copernicus Emergency Management Service. The photos (Fig. 3b–f) demonstrate the inability of most infrastructure assets to withstand this flood, irrespective of the structural characteristics and construction age. It is worth mentioning that the latter ranged substantially, from 23 years (Br7, Fig. 3b) to 70 years (Br8, Fig. 3b). Common failure patterns include:

i) Extensive damage of abutments, with partial or complete wash away of backfill, indicating extreme peak discharges along Pamissos and its secondary streams.
ii) Substantial scouring of foundations, leading to deformations and collapse of piers of the older structures that were supported on shallow foundations (Fig. 3c, e).
iii) Significant debris built up contributing to failure especially in the case of intermediate piers.

Indicative of the extreme magnitude of erosive forces that impacted the riverbanks of Pamissos is the 2 m deep scour hole that exposed the piled foundation of the NW abutment of Br7, a relatively modern motorway bridge. Incidentally, the bridge was inspected only two months before the event and was found intact (Mitoulis et al., 2021), which suggests that the massive scour hole was the result of this single flood.

1.2. The Bridge 9 failure

A 12 m long and 8 m wide gap was observed after the flood along the road that connects Mouzaki to Ellinokastro, because of a bridge failure (Fig. 4a–b). The structure was constructed in the 1960s and no drawings or other official information regarding its design are available. Post-flood visual inspections revealed that the bridge consists of (i) a 20 m long deck with a continuous reinforced concrete (RC) slab integrally cast in situ with four precast beams, (ii) three diaphragm beams, one at the mid-span

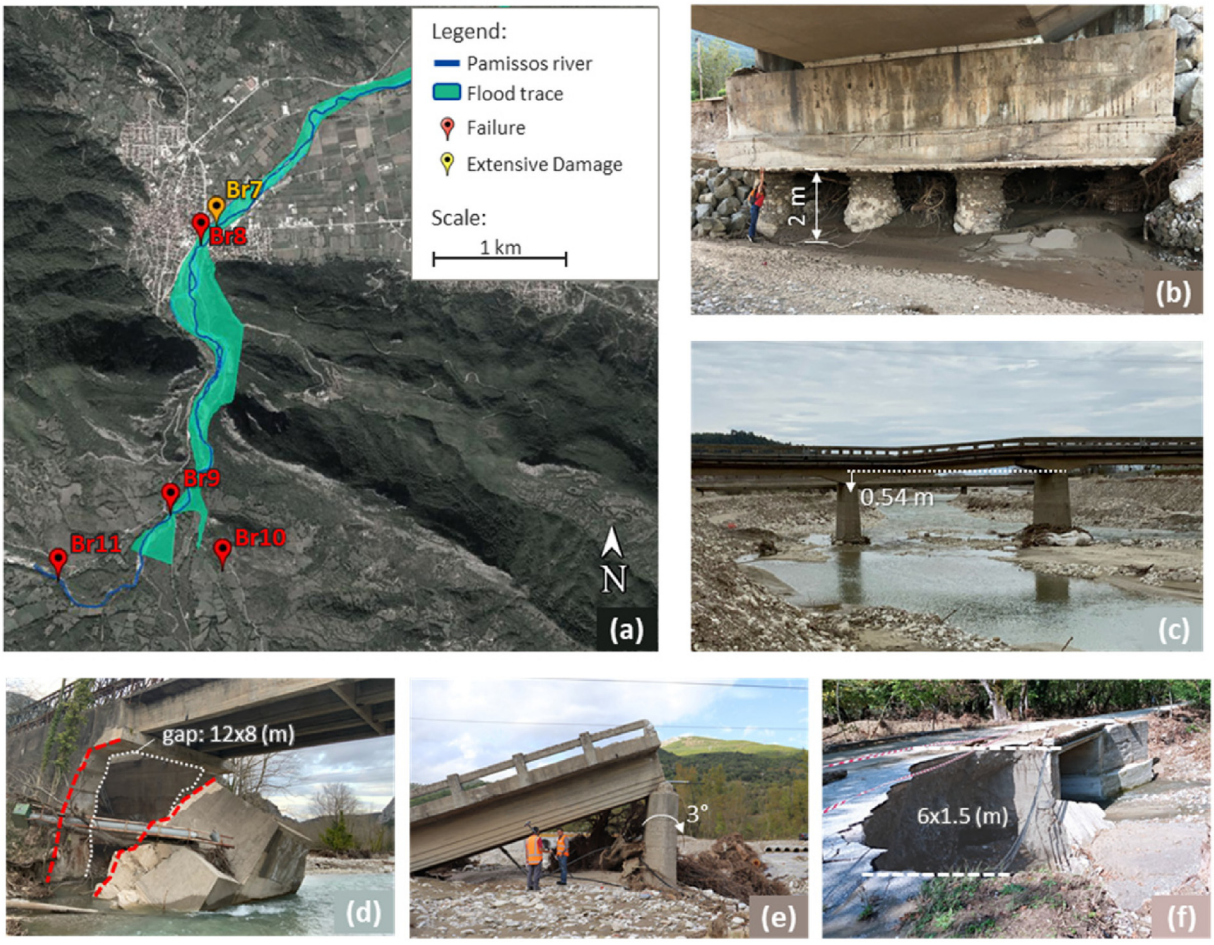

Fig. 3. Impact on bridges: (a) map of flood trace in the area of Mouzaki showing the situation on 24/09/2020 (5 days after the event) as per the post-event assessment by the E.U. Copernicus Emergency Management Service, with locations and photos of severely damaged bridges along Pamissos river (flowing from South to North) and its secondary streams: (b) Br7; (c) Br8; (d) Br9; (e) Br 11; and (f) Br 10.

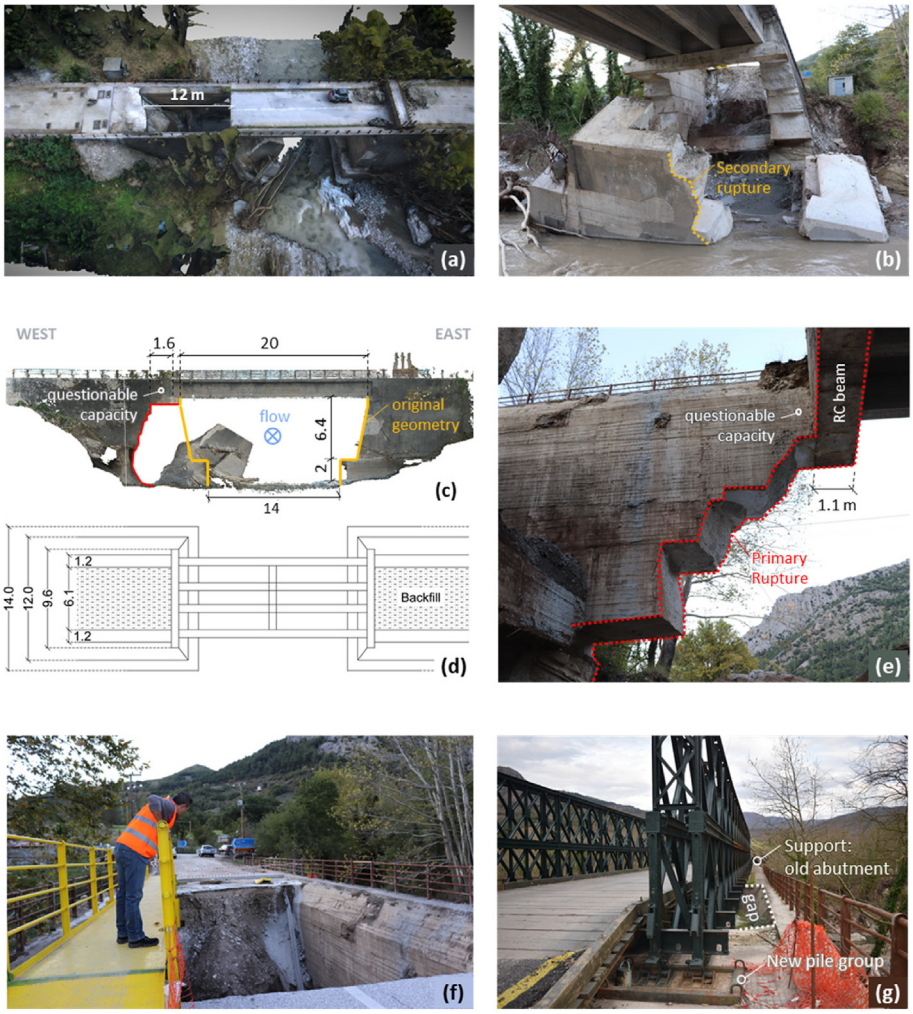

Fig. 4. Bridge 9: (a) 3D mesh model constructed using UAV images; (b) photo of the fractured unreinforced concrete abutment; (c) elevation and (d) plan view; (e) closer view of the failure pattern at the northern (downstream) wall; and (f) photo of the temporary emergency passage on 14 October 2020; and (g) the mitigation solution including the construction of a Bailey bridge on 28 November 2020.

and two at (iii) the massive abutments. The latter consist of 8 m tall, Π-shaped gravity wingwalls that retain the backfill (Fig. 4c). The wingwalls are made of unreinforced concrete.

According to testimonies, a scour hole of substantial size was evident around the foundation of the western abutment before this flood. As indicated by the following numerical results, this loss of support undermined the capacity of this abutment, as opposed to the opposite (eastern) structure, contributing to the rupturing of its concrete walls and the detachment of the part that collapsed. The remaining part of the walls reveals the shape of the primary rupture (Fig. 4d), which includes a full-height crack that propagates on both sides of the abutment (upstream and downstream). The abutment collapse was accompanied by the complete wash-out of the backfill carrying away the overlying roadway.

The impact of the above failure was significant on the local communities. Traffic interruption lasted over 60 days. During this time the commuters of nearby villages (in their majority elderly people) did not have access to essential facilities and services that are available in Mouzaki. In the first few days after the event, an emergency pedestrian bridge (Fig. 4f) was installed at the deck, to allow the crossing of the river by pedestrians only. However, it was quickly removed due to significant concerns over its safety. The unknown capacity of critical remaining bridge segments (highlighted in Fig. 4c–e) due to the complete lack of information regarding their design, was the key concern that led to this decision.

Traffic was restored at the end of November 2020, after the installation of a Bailey bridge over the old structure. The new bridge support relies on the standing eastern abutment (Fig. 4g). As such, concerns remain regarding the longevity of this mitigation solution.

In response to the urgent need to understand the condition of the asset, we carried out a comprehensive diagnostic investigation that sheds light on the safety and flood resilience of the new structure. We place our focus on Br9 because:

1. It is in a strategic location: at a relatively short distance upstream of Mouzaki, and with no significant stream junctions in-between. An estimate of flow intensity at this cross-section of the river will provide a valuable boundary condition for hydraulic (and other) studies dealing with the assessment/prediction of the flood conditions that caused the extensive damage of the downstream infrastructure and ecosystem.
2. The failure mechanism is relatively straightforward. Dominated by the material response of concrete, it can be characterized and simulated with lower uncertainties in comparison to more complex cases where less standardized materials are involved.
3. It is representative of a common and highly vulnerable class of the bridge stock existing in Greece and in the Balkans: single-span bridges on rigid bank-line (instream) supports. Insights on its vulnerability to flooding associated hazards will be a useful guide in vulnerability and risk assessments considering similar bridges.

In-stream abutments induce contraction of the flow triggering a highly turbulent and complex, 3D flow field (Chrisohoides et al., 2003;

Kara et al., 2015; Vui Chua et al., 2019). The associated bed shear stresses give rise to local scour mechanisms that have been investigated in several experimental and numerical studies, e.g.: (Melville, 1992; Sturm and Janjua, 1994; Oliveto and Hager, 2002; Teruzzi et al., 2009; Yorozuya and Ettema, 2015; Afzal et al., 2020). However, the focus of this paper is not on scour evolution directly, but rather on its role as an additional factor that increases flood hazard vulnerability. The latter has received little attention, with the majority of studies considering it as an extension to earthquake or multi-hazard vulnerability (e.g. Ahamed et al., 2020; Argyroudis and Mitoulis, 2021; Argyroudis et al., 2020; Alabbad et al., 2021). While previous studies place their emphasis on scour development, this study highlights the need to incorporate the potentially major component of hydrodynamic actions in sites where high velocity flows are likely to occur (e.g., due to flash flooding) to achieve a comprehensive description of bridge vulnerability to flood hazards.

2. Field surveys

2.1. UAV aerial mapping

As per the framework proposed in Fig. 1, Unmanned Aerial Vehicles (UAVs) are used to develop 3D models of the target infrastructure. Sensor equipped UAVs are increasingly used in the infrastructure field and their applications are only expected to increase (Greenwood et al., 2019). Most commonly optical cameras are used for infrastructure assessment. Thanks to technology advancements, other sensor payloads, such as Light Detection and Ranging (LiDAR) (Teng et al., 2017; Bolourian and Hammad, 2020), infrared or hyperspectral cameras (Nishar et al., 2016), sensors for air quality (e.g., Rossi and Brunelli, 2016), or even wireless sensor networks (e.g., Jawhar et al., 2014; Ho et al., 2015) are selectively deployed. UAVs are becoming particularly valuable tools for post-disaster reconnaissance and collection of perishable data immediately after a disaster, due to their ease of use and the ability to collect high-quality data remotely and safely (Zekkos et al., 2016; Bray et al., 2019; Wartman et al., 2020). Naturally, the use of UAVs has greatly enhanced the potentials of rapid bridge inspection and structural health assessment, overcoming the drawbacks of manual visual inspection (Chen et al., 2019; Lei et al., 2018; Chan et al., 2015).

The use of UAV mapping in this study was essential in enabling the rapid collection of perishable data, necessary for the interpretation of failure. Crucially, it allowed for a thorough site reconnaissance and mapping of a complex three-dimensional target, such as a failed bridge, with maximum safety, while the integrity of structural remains was under investigation. The produced 3D model was useful for: (i) Measurement of the geometric features of the structural components, and production of an idealized 3D geometry for use in the numerical analyses; (ii) Measurement of channel width and depth for use as input in the analysis of water flow; (iii) Identification of the joints and reproduction of these, as interfaces, in the mechanical model; (iv) Mapping of the observed rupture path for comparison with the numerically computed failure patterns; (v) Confirming that the eastern, standing, abutment showed no measurable deformation and damage was concentrated on the failed abutment (West).

For the 3D mapping of the bridge and the surrounding area, a DJI Phantom 4 Professional (P4P) quadcopter was deployed. The UAV operates with an integrated optical camera coupled to the UAV through a triaxial gimbal, serving as a stabilizer for shake-free footage. Some characteristics of the P4P UAV platform and integrated camera are outlined in Table 1.

2.2. Image collection and processing

The field team carried out aerial and terrestrial mapping works on 14 and 15 October 2020, which included on-site identification of the study areas, UAV mapping flights, and ground control points topo survey for verification.

The objective of UAV data collection was the creation of a 3D model using the Structure-from-Motion (SfM) technique (Snavely et al., 2008; Zekkos et al., 2018), which involved the collection of overlapping optical imagery data. Still, oblique photos (facing towards the ground, camera axis 45 degrees from vertical) following a fully autonomous double grid lawnmower-type pattern and maintaining 80% frontal overlap (with respect to the flight direction) and 80% side overlap (between flying tracks) were collected as shown in Fig. 5a–b. Due to the complex geometry of the bridge structure, the autonomously-collected photos were complemented by additional aerial photos captured while manually operating the UAV. These were needed to eliminate "shadow" or occluded areas and ensure the creation of a complete and accurate bridge model.

Table 1
UAV and camera specifications used in this study.

Phantom 4 Professional UAV	
Take-off weight	1.38 kg
Diagonal size	35 cm
Maximum velocity	20 m/s
Maximum flight time	25 min
Integrated P4P camera	
Sensor size	1 in. (20 M)
Maximum aperture	f/2.8
FOV	84°
Maximum photo resolution	5472 × 3648 Pix
Maximum video resolution	4096 × 2160 Pix

SfM software, specifically Bentley's Contextcapture, was used to process the collected imagery and generate a 3D Point Cloud of the bridge. SfM combines the benefits of photogrammetry and computer vision to reconstruct a 3D scene by identifying matching features in multiple images. Internal (camera focal length, image sensor format, principal point) and external camera parameters (positions and orientations) are automatically calculated by the software's matching algorithm routine, resulting in an initial sparse 3D point cloud. Because initial calculated values suffer from lens distortion faults, ground control points (GCPs) surveyed with centimeter-level accuracy are implemented in the process to refine internal and external camera parameters and introduce georeferencing information to the 3D reconstructed geometry.

A total of 606 images (Fig. 5) were collected at a flight altitude ranging from 10 to 40 m resulting in a mean ground sampling distance (GSD) of 0.78 cm/pixel. For data quality verification and precise georeferencing of the collected data and spatial products reconstruction, 13 GCPs and check points (CPs) were surveyed with a survey-quality GNSS receiver, spatially covering the areas mapped (Coordinate system used GGRS87/Greek Grid – EPSG:2100). A selection of the collected points was used as check points to assess the quality of the 3D model (Fig. 5c). Also, 11 additional manual tie points were initialized to combine autonomous and manual flights' images and reconstruct a unified 3D model with detail added in occluded parts of the bridge. The resulting 3D error estimates ranged between 2.1 and 4.8 cm with a mean reprojection error for the point cloud at 0.53 pixels.

Fig. 5e–f displays views of the 3D mesh showing the collapsed abutment. A 3D visualization of the bridge model is freely available online (https://skfb.ly/6VXHW) to facilitate understanding of the failure pattern.

2.3. Characterization of abutment material and in-situ testing

The failure of the abutment was due to fracture (and then collapse) of its unreinforced concrete walls. Modelling of the concrete material behaviour, with as much accuracy as possible, was key in reproducing the observed failure pattern. Given the age of the structure and the complete lack of design information, a field investigation was carried out to characterize the effective strength of the material following the European standards for in-situ assessment of concrete (CEN, 2019). A total of six cores were extracted from representative locations and heights of the collapsed part of the abutment (Fig. 6) and tested in compression. Table 2 lists the geometrical characteristics of the tested cylinder specimens and respective concrete strength parameters. The measured in-situ compressive strengths (f_{is}) were converted to characteristic strengths of the standard 150 mm × 300 mm cylinders

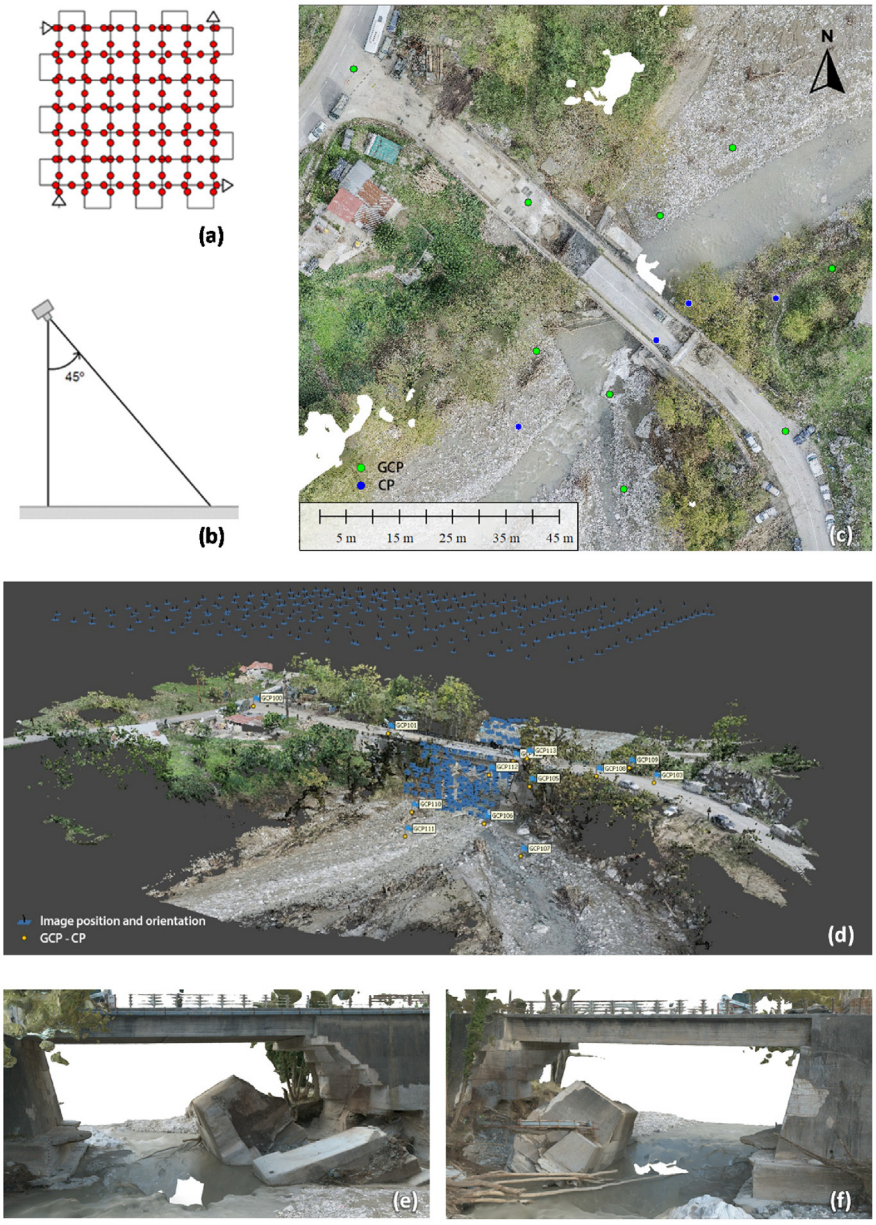

Fig. 5. (a) Schematic of a double-grid lawnmower-type flight pattern, (b) schematic of oblique camera orientation used during data acquisition, (c) top view orthophoto with GCPs and CPs, (d) 3D point cloud perspective view illustrating GCPs/CPs as points and images' positions/orientations as blue polygons, (e) 3D mesh NE view, (f) 3D mesh SW view.

Fig. 6. Photos of core extraction locations.

and 150 mm × 150 mm cubes ($f_{is,cylind}$ and $f_{is,cube}$, respectively) using the locally valid size conversion factors (i.e. Greek standards).

The in-situ characteristic strength was estimated as:

$$f_{ck,is} = min \left\{ \begin{matrix} f_{m(j),is} - k \\ f_{lowest,is} + 4 \end{matrix} \right\} \quad (1)$$

Table 2
In-situ compression test results.

No.	D (mm)	H/D	f_{is} (MPa)	$f_{is,cylind}$ (MPa)	$f_{is,cube}$ (MPa)
1	956	0.99	50.4	40.8	46.5
2	956	1.06	44.1	36.4	41.9
3	957	1.04	31.9	26.2	30.9
4	958	1.05	35.0	28.8	33.8
5	957	1.07	27.7	22.9	27.4
6	957	1.06	22.3	18.4	22.7

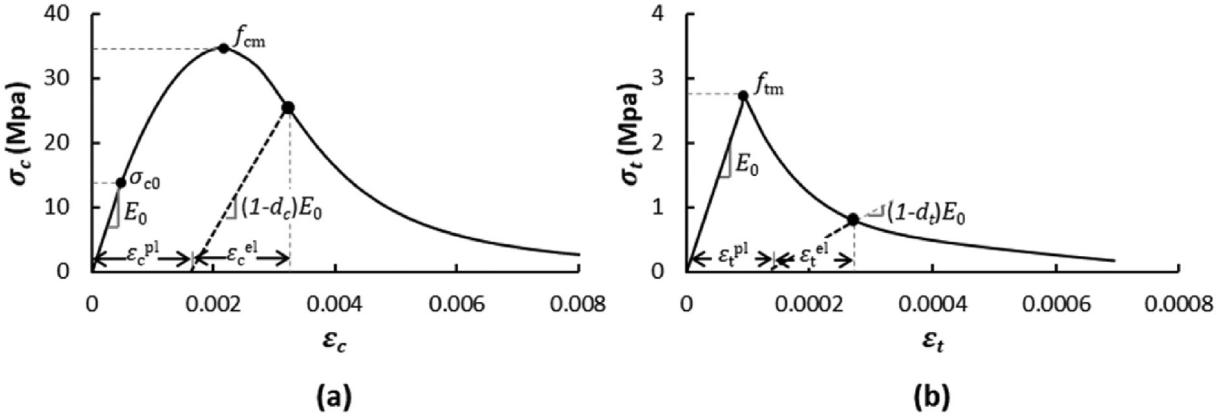

Fig. 7. Assumed stress – strain behaviour of concrete in (a) compression and (b) tension.

where, $f_{m(j),is}$ and $f_{lowest,is}$ are the mean and the lowest values, respectively, of the estimated in-situ cube strengths, j is the number of cores, and $k = 7$ (effective for $3 < j \leq 6$).

Nonlinear uniaxial stress – strain material response curves where generated (Fig. 7) following the closed form solutions proposed by Alfarah et al. (2017), assuming $f_{cm} = f_{ck} + 8$, $\varepsilon_{cm} = 0.0022$, and $f_{tm} = 0.3016\, f_{ck}^{2/3}$, according to the fib Model Code for Concrete Structures (CEB-FIP, 2010).

3. Numerical methods

This study combines nonlinear structural Finite Element (FE) analysis of the affected bridge in conjunction with 3D Computational Fluid Dynamics (CFD) simulation to define the loading conditions that likely caused the failure of the bridge abutment. The results are then used to determine the minimum flow intensity necessary to cause the observed damage.

3.1. FE analysis and structural damage interpretation

3.1.1. Materials and boundaries

Hexahedral, 8-node continuum elements (type: C3D8R) were used to reproduce the 3D geometry of the bridge and the surrounding ground in the ABAQUS FE code. Fig. 8a shows details of the FE mesh indicating the various materials considered:

- The reinforced deck, which after a visual inspection was found to be undamaged, was assigned typical elastic properties for reinforced concrete.
- On the contrary, the cracked walls of the abutment were modelled by nonlinear finite elements using the Concrete Damage Plasticity (CDP) constitutive model, while considering the presence of construction joints, as discussed in the following.
- The top segments of the abutment walls (highlighted in Fig. 8a as questionable sections) were a key safety concern, as discussed previously. Acting as horizontal beams that connect the remaining deck to the abutments, they became critical for the overall stability when the collapse left part of them unsupported (Fig. 4c–e). Having no information on their design, we considered two different scenarios: (i) these sections are reinforced (assigned the elastic properties of reinforced concrete) or (ii) they have no reinforcement, similar to the abutments. All the simulations discussed in the following were, in fact, carried out for both scenarios (i) and (ii). However, scenario (ii) proved unrealistic, leading to damage patterns that were inconsistent with observations. As such, the following presentation of results is restricted to scenario (i). This investigation could be extended to parametrically consider likely reinforced concrete designs (simulating typical reinforcement ratios). However, this would be a computationally costly endeavour, due to the degree of refinement necessary for rebars to be modelled. As the exact capacity of the specific sections does not affect the estimated critical flow velocity, provided that the presence of reinforcement is enough to keep them intact, a detailed investigation of their response was deemed to be out of the scope of this study.
- In the nonlinear domain, soil response was simulated by the elastoplastic Mohr–Coulomb constitutive model. A 10 m deep layer of uniform sand was considered. Material response properties were determined with respect to the geotechnical data available for another bridge, located downstream (namely, Br7 (Zekkos and Zalachoris, 2020)). Pre-yield behaviour is approximated using a secant shear modulus $G_s = 45$ MPa (assuming $G_s/G_0 = 0.5$, i.e. medium strain domain); failure is described by the soil friction angle $\varphi = 37°$and the apparent cohesion $c = 10$ kPa. Although the soil is presumed to be fully saturated, the effect of pore pressures cannot be considered explicitly as the analysis is conducted in a total stress environment. To indirectly alleviate this error, the soil is assigned a reduced, effective friction angle (φ') calculated based on shear strength similarity under geostatic conditions: $\frac{\tan(\varphi')}{\tan(\varphi)} = \frac{\gamma_s - \gamma_w}{\gamma_s}$, where γ_s is the saturated soil unit weight and γ_w is the unit weight of water. This is a rough approximation of soil behaviour, affordable because, according to a sensitivity analysis discussed in the following, the observed bridge failure mechanism is not sensitive to the deformability of the supporting soil.
- The same material modelling strategy was adopted for the simulation of the backfill, assuming typical properties for gravel (Tito, 2019), namely: Young's Modulus $E = 150$ MPa; friction angle $\varphi = 42°$; dilation angle $\psi = 12°$; apparent cohesion $c = 40$ kPa.

Soil–footing and backfill–abutment wall interfaces are modelled with contact elements allowing detachment and sliding (with a friction coefficient $\mu = 0.5$). Displacements (δ) of the bottom boundary (assumed bedrock) are restrained in all directions. Symmetry-type boundary conditions are applied at the sides of the model that are perpendicular to the flow. On the other hand, the parallel to the flow sides follow different boundary conditions depending on the computational step: the initial requirement for zero displacements in the y direction ($\delta y = 0$), effective during accommodation of self-weights (gravity loads), is complemented with a requirement for zero displacements in every direction (fixity) in the subsequent scouring and hydrodynamic loading steps. The latter is due to the abutment wingwalls being practically anchored in the riverbank soil, extending for about 15 m beyond the post-flood channel crest.

Fig. 8a also defines the coordinate system adopted, i.e., through the positive x-axis indicates the direction of the channel flow (streamwise direction). The y axis aligns with the longitudinal axis of the bridge (spanwise direction), while the z-axis points to the upward vertical direction.

3.1.2. Concrete damage plasticity (CDP)

The CDP constitutive model (Lubliner et al., 1989; Lee and Fenves, 1998) is readily available within the Abaqus FE code (SIMULIA, 2014). It is a continuum, plasticity-based, damage model where failure is associated with two prevailing mechanisms, i.e., tensile cracking and compressive crushing. It has been effectively adopted in several numerical studies of

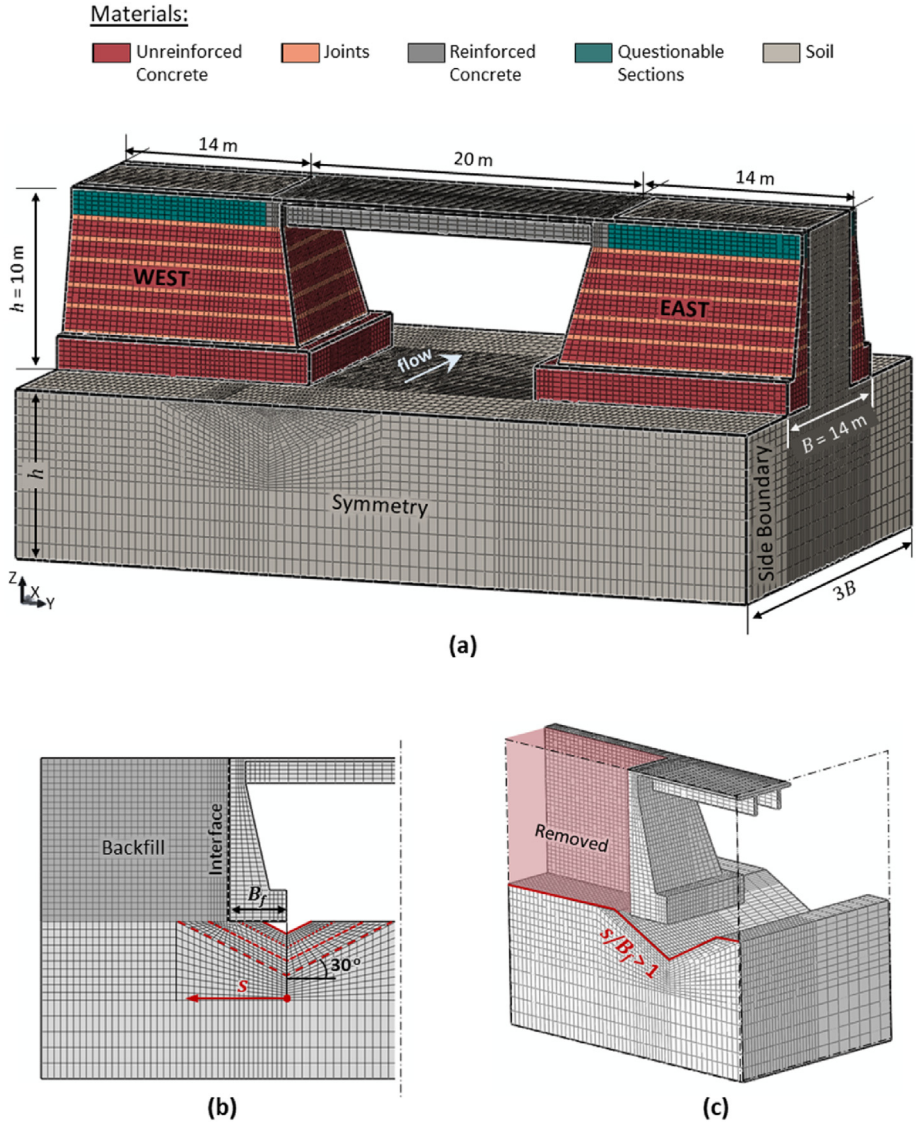

Fig. 8. 3D FE model (Model A) used in the mechanical analysis of scouring effects: (a) materials, selected dimensions, and boundaries; (b) abutment elevation and closer view of the scour hole geometry, and (c) 3D model: simulation of backfill loss (showing a quarter of the model).

the nonlinear response of concrete structures in monotonic, cyclic, and dynamic loading (e.g. Antoniou et al., 2020; Agalianos et al., 2020; Krahl et al., 2018; Behnam et al., 2018).

Post yield behaviour is described with respect to equivalent plastic strains in tension and compression, ε_c^{pl} and ε_t^{pl}, by means of stress – strain material response curves customised by the user (Fig. 7). The damage variables d_c and d_t control the unloading – reloading response defined according to (Alfarah et al., 2017) as:

$$d_c = 1 - \frac{1}{2 + a_c}\left[2(1 + a_c)\exp\left(-b_c e_c^{ch}\right) - a_c \exp\left(-2b_c e_c^{ch}\right)\right] \quad (2)$$

$$d_t = 1 - \frac{1}{2 + a_t}\left[2(1 + a_t)\exp\left(-b_t e_t^{ck}\right) - a_t \exp\left(-2b_t e_t^{ck}\right)\right] \quad (3)$$

where e_c^{ch} and e_t^{ck} are the crushing and cracking strains, respectively, while coefficients α and b are calculated as follows:

$$a_c = 7.873; a_t = 1;\ b_c = \frac{1.97 f_{cm}}{G_{ch}} l_{eq};\ b_t = \frac{0.453 {f_{ck}}^{2/3}}{G_{ch}} l_{eq} \quad (4)$$

G_f and G_{ch} are the fracture and crashing energies per unit area, defined as:

$$G_f = 0.073 {f_{cm}}^{0.18} \quad (5)$$

where f_{cm} is in MPa, and

$$G_{ch} = \left(\frac{f_{cm}}{f_{tm}}\right)^2 G_f \quad (6)$$

The characteristic element length l_{eq} is introduced in the description of the damage to mitigate mesh dependency effects that typically arise when strain localization problems associated with material softening are modelled using finite elements. The adopted mesh regularization technique relies on the scaling of both fracture and crushing energies in relation to the finite element size, following the well-established Crack Band Method (Bažant and Oh, 1983). The main underlying assumption is that damage is localized in a single row of elements, which is a reasonable assumption in cases where the response is dominated by fracture, as in the problem investigated herein. Here, l_{eq} has been kept constant and equal to 300 mm, except for the trapezoidal section of the wing-walls where it unavoidably varies from 203 mm to 373 mm. Nevertheless, the latter is a region where we do not expect strain

localization, according to field observations, and as such, this local deviation from mesh uniformity is believed to be of reduced importance for the computed failure path.

Additional material constants necessary for the formulation of CDP have been defined according to typical values suggested by Alfarah et al. (2017):

- The dilatancy angle: $\psi = 13^{o}$. This is rather a lower bound value for concrete, assumed appropriate for the considered weathered material.
- The flow potential eccentricity: $\epsilon = 0.1$.
- The ratio of initial biaxial compressive yield stress to the initial uniaxial compressive yield stress: $\sigma_{bo}/\sigma_{co} = 1.16$.
- The ratio of second stress invariants on tensile and compressive meridians: $K_c = 2/3$.

3.1.3. Response of construction joints

Preliminary simulations revealed that modelling of the "weak" zones resulting from the existence of smooth construction joints is essential for the reproduction of the failure plane pictured in Fig. 4e. These construction joints have no reinforcement passing through them and as a result, their response is one of blocks of concrete seating upon each other and relying on friction for the transmission of any lateral loads. Following the model proposed by Clark and Gill (1985), joint planes were associated with a modified Mohr-Coulomb failure criterion with zero tensile strength. Consistently with their recommendation, effective for unreinforced construction joints in concrete prisms with cube strength 24–66 MPa, the characteristic shear strength is calculated as

$$\tau = 0.07 f_{cm} + 0.75\sigma \tag{7}$$

Indeed, observation of the intact, eastern abutment (Fig. 9) indicates a response dominated by shear with minimal, yet evident, permanent sliding displacements accumulated upon its exposed joints.

3.1.4. Progressive scouring

Following the paradigm of recent numerical and experimental studies on the effect of scouring on the mechanical response of structures (Tubaldi et al., 2018; Scozzese et al., 2019; Zhang et al., 2019; Ciancimino et al., n.d.), we approximate scour development by the generation of a hole under and around the foundation (local scour). The progressive expansion of the scour hole was implemented in consecutive steps and parameterized with respect to the penetration parameter s (Fig. 8b). Importantly, when s becomes equal to the width of the footing (B_f), the stability of the backfill is undermined due to erosion, even if the concrete walls remain standing.

Fig. 9. Photo of the standing, east, abutment with evident relative displacements at the interfaces between concrete blocks, indicating that the joints act as weak zones.

Therefore, we assume complete loss (removal) of the backfill, when $s/B_f > 1$, as shown in Fig. 8c.

In reality, scour holes form asymmetrically, along both x and y directions, while their exact morphology is known to depend on the flow characteristics (depth and velocity), the geometry of the abutment, and the geotechnical properties of the soil (Oliveto and Hager, 2002; Melville, 1997; Zhang et al., 2018). Being unable to inspect the actual scour hole, as it was covered by debris from the partially collapsed abutment, we assumed an idealized geometry, considering a symmetric conical trench with slope angles equal to the critical state friction angle and uniform depth in the streamwise (x) direction (Fig. 8b). This modelling approach is in agreement with experimental findings (Ciancimino, 2021) showing that it is essential to model the localized nature of scour, as opposed to assuming removal (erosion) of uniform soil layers. Based on results from centrifuge model tests on scour affected piers (Ciancimino et al., n.d.), we estimate that deviations from the exact slope gradient of the hole will have a minor impact on the mechanical response of the bridge and the computed failure mechanism.

Aiming to further boost computational efficiency (useful for the subsequent analysis of hydrodynamic loads) we investigate the effectiveness of a simplified model in reproducing scour-induced damage. Taking advantage of the fact that the studied failure is governed by the response of concrete, and soil plays only a secondary role, the reduced model (Model B) reproduces the structural parts of the original model (Model A) while accounting for soil resistance by means of translational and rotational springs, as shown in Fig. 10a–b. Elastic, effective stiffness coefficients (k') for movement in every direction are computed based on the expressions developed by Gazetas (Gazetas, 1983) considering the effective (i.e. supported) area of the foundation and $G_s = 0.5G_0$.

Fig. 10c plots the evolution of foundation settlements with increasing s/B_f (with reference to the top, centre point of the footing). Model B underestimates displacements in comparison to Model A, owing to its linear-elastic formulation. Nevertheless, both models predict relatively low displacements without any signal of collapse being imminent, even when $s = 2B_f$. Comparison in terms of structural damage due to scouring (when $s = 2B_f$), as reflected in the contours of maximum principal strain shown in Fig. 11, shows that Model B adequately captures the structural deformation pattern. Although it predicts somewhat lower deformations at the joints of the abutment (i.e. openings), the response of the concrete blocks remains elastic in both Models (with $\varepsilon_t < \varepsilon_t^{el}$, see Fig. 7b).

Importantly, Fig. 11 demonstrates that the concrete walls of the abutment can safely bear the weight of the structure even when they are extremely exposed, under the assumption of a massive scour hole ($s/B_f \approx 2$). As such, we may conclude that scouring, alone, could not have caused the dramatic failure of Br9. This led us to seek and investigate new mechanisms of this bridge failure considering scouring in conjunction with hydrodynamic loads. These mechanisms were sought based on the compatibility of the observed failure with the river channel geometry, the flow intensity, and the parts of the bridge that were found to have been detached. To this end, we used FE Model B paired with CFD modelling.

3.1.5. Hydrodynamic loading of the deck

Field inspections showed that the deck of the bridge was fully submerged during the peak of the flood, in agreement with testimonies. The surrounding fields were covered by approximately 1.5 m of water, yet there is no measure of the water table level at the location of the deck.

When submerged, decks are subjected to dynamic actions that can lead to failure (Chen et al., 2009; Oudenbroek et al., 2018; Greco et al., 2020). The quantification of these actions for riverine bridges has been the purpose of several studies (Jempson, 2000; Malavasi and Guadagnini, 2003; Malavasi and Guadagnini, 2007; Kerenyi et al., 2009). Drag, lift, and

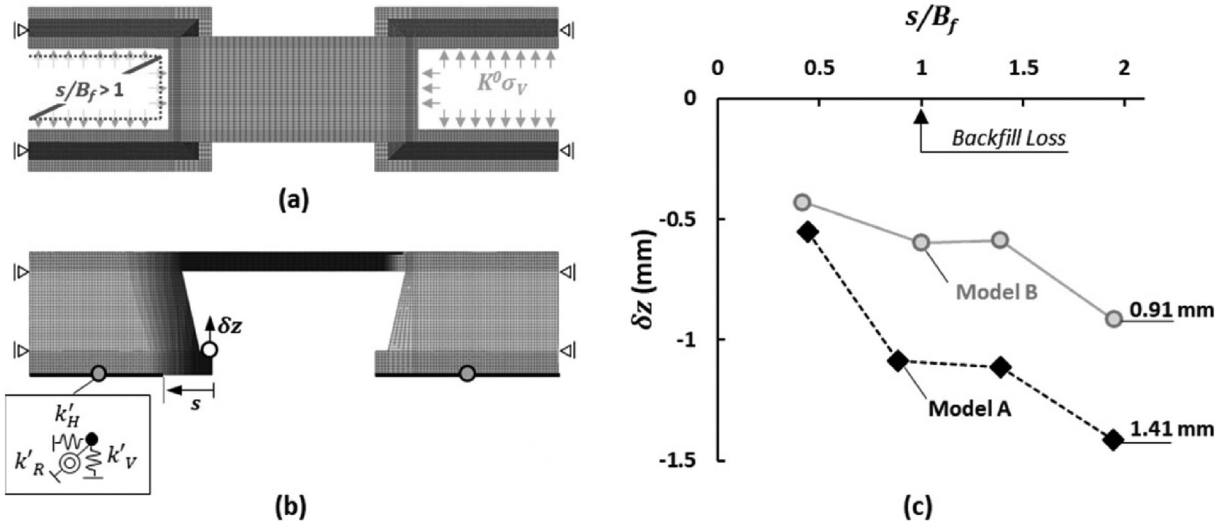

Fig. 10. Modelling of scour hole evolution: (a) plan and (b) side view of simplified model B; (c) comparison with settlements predicted by Model A with reference to the mid-point of the abutment footing.

moment loads (F_D, F_L, and F_M, as defined in Fig. 12a) are typically presented in non-dimensional forms in terms of the respective coefficients:

$$C_D = \begin{cases} \dfrac{F_D}{\frac{1}{2}\rho V^2 L d}, \ if\ h^* \geq 1 \\ \dfrac{F_D}{\frac{1}{2}\rho V^2 L (h_u - h_d)}, \ if\ h^* < 1 \end{cases} \quad (8)$$

$$C_L = \frac{F_L}{\frac{1}{2}\rho V^2 L W} \quad (9)$$

$$C_M = \frac{F_M}{\frac{1}{2}\rho V^2 L} \quad (10)$$

where C_D, C_L, and C_M are the drag, lift, and moment coefficients, respectively. V is the mean upstream flow velocity; ρ is the water density; L, W, and d are the length, the width, and the total height of the deck, respectively; h_u is the total water depth upstream of the bridge and h_d is the height of the deck from the bottom channel boundary; while h^* is a dimensionless inundation index defined as:

$$h^* = \frac{h_u - h_b}{d} \quad (11)$$

The inundation index is a key parameter due to the asymmetry of flow around decks, as local, wave-type distortions of the free water surface occur in the proximity of the structure (Malavasi and Guadagnini, 2007). Deck load coefficients depend also on various other parameters, notably the shape of the submerged structure (W/d); its proximity to the bottom boundary (h_d/d); and the characteristics of the flow, typically accounted for by means of the Froude number (F_r):

$$F_r = \frac{V}{\sqrt{g h_u}} \quad (12)$$

where g is the gravitational acceleration.

Available in the literature are charts that parameterize the average value of C_D, C_L, and C_M as a function of h^* and can be used for calculation of the respective loads acting on decks, assuming steady-state flow. This study has adopted the relationships proposed by Kerenyi et al. (2009) who carried out experiments and numerical simulations considering

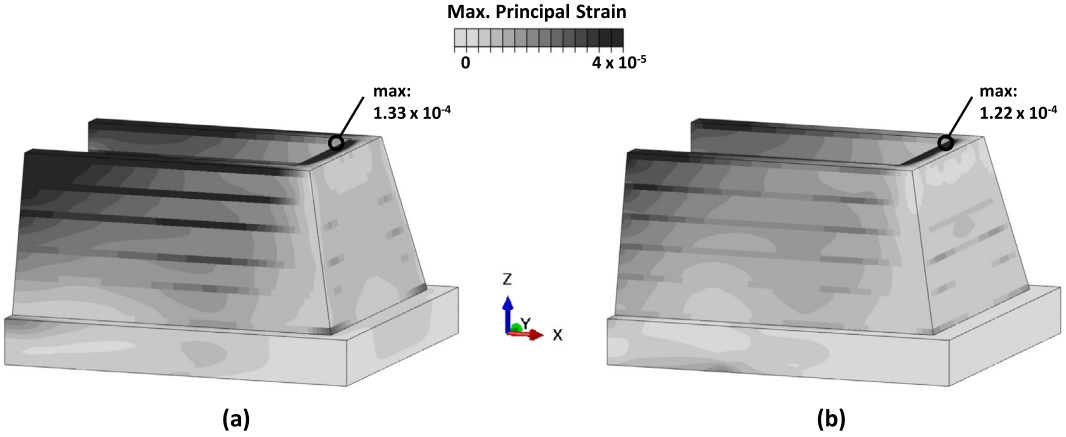

Fig. 11. Plastic strains developed at the concrete walls of the abutment for $s/B_f = 1.94$ in (a) the full model (model A), compared to (b) the bridge-on-springs model (model B).

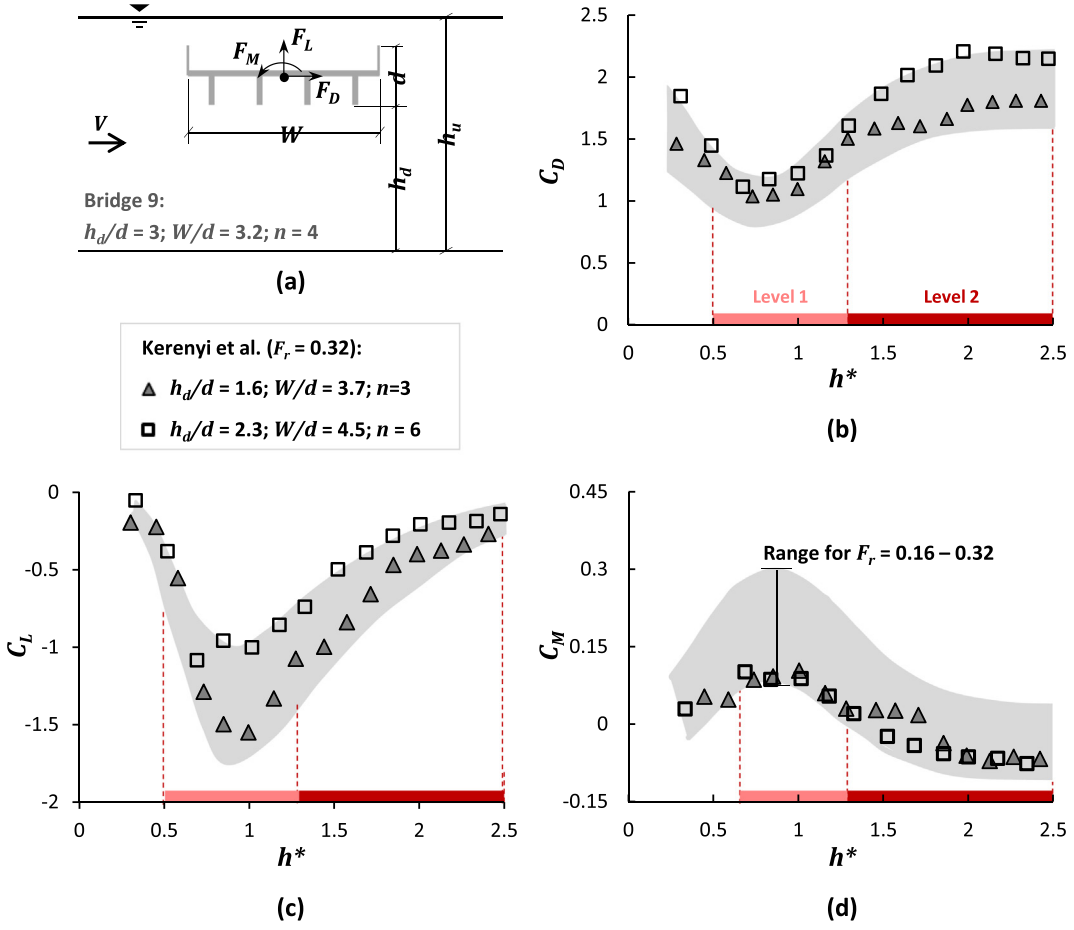

Fig. 12. Average (steady-state) hydrodynamic loads on girder decks: (a) nomenclature; and coefficients of (b) drag; (c) lift; and (d) moment, measured on model decks submerged in flows characterized by F_r = 0.16–0.32 for varying inundation heights (h^*).

model decks that quite resemble the slab-on-girders configuration of our structure. Fig. 12 summarizes experimental results for three- girder (n = 3) and six- girder (n = 6) decks submerged in flows with F_r = 0.32, the maximum F_r considered in (Kerenyi et al., 2009). Also shown in the figure are envelopes around results for various flow regimes and for F_r ranging from 0.16–0.32. This corresponds to water velocities in the range of 1.5–3.9 m/s. We should note that the flow velocity upstream of Br9 probably exceeded this range. Yet, we consider the above as a representative flow intensity field and use the envelopes of Fig. 12 to estimate deck load coefficients for two probable levels of water height:

- Level 1: Moderate inundation ($0.5 < h^* \leq 1.3$)
  $C_D^{(1)} = 1.2$; $C_L^{(1)} = -1.5$ (signifying downward push); and $C_M^{(1)} = 0.3$.
- Level 2: Heavy inundation ($h^* > 1.3$)
  $C_D^{(2)} = 2.2$; $C_L^{(2)} = -0.5$; and $C_M^{(2)} = -0.06$.

3.2. Abutment–flow interaction

3.2.1. CFD modelling

Flow around the abutment is modelled in three dimensions. The geometry of the abutment is reproduced, based on the 3D model. The river channel is modelled in a simplified manner considering a rectangular cross-section (Fig. 13). Reynolds averaged Navier-Stokes (RANS) analysis is carried out using the finite volume method in the general-purpose CFD code ANSYS Fluent. Boundary conditions include a unidirectional inlet flow and a zero-gauge pressure outlet. They are imposed at a distance of 5 W and 10 W upstream and downstream of the abutment, respectively, where W is the total abutment width, to model a total channel length of 224 m (Fig. 13b) and minimise the effect of boundaries.

The mid-stream symmetry plane allows modelling of half of the channel width. No-slip boundary conditions are assigned to the walls of the abutment. Likewise, the channel bottom and its sidewalls are treated as stationary wall boundaries. Employing single-phase modelling, we adopt the "rigid lid" boundary condition for modelling the interface between water and air (i.e. the water surface, denoted as "sky" in Fig. 13a). This implies a von-Neuman slip condition for the tangential to the surface direction and a zero-velocity requirement in the direction normal to the water surface. Despite being the most common treatment of the water surface in CFD studies of open channels (Chrisohoides et al., 2003; Teruzzi et al., 2009), this approximation has known limitations as it cannot reproduce local flow accelerations and water surface deformations, particularly near the edges of the abutment (Kara et al., 2015).

Due to the geometry of the problem and the anticipated level of flow velocity, we have considered a highly turbulent flow field, represented by blockage Reynolds numbers in the range $1 \times 10^6 < Re \leq 1 \times 10$ (Marchi et al., 2010). The blockage Reynolds number, $Re = {}^{VB_f}/_{\nu}$ (where ν is the kinematic viscosity), hereinafter simply called Reynolds number Re, refers to the width of the abutment that blocks the flow (B_f). The realizable k-ε eddy-viscosity model (Shih et al., 1995) is used to simulate turbulent flow. The wall function method (Launder and Spalding, 1983) is employed to account for near-wall response, where the viscous effects dominate over turbulence. After a preliminary sensitivity study considering the four different wall function models available in Fluent (Fluent Theory Guide, 2013), we selected the scalable wall function as the most suitable for the highly non-uniform grid of tetrahedral elements that we use to discretize the fluid domain (Fig. 14). The validity of this modelling approach was subsequently judged

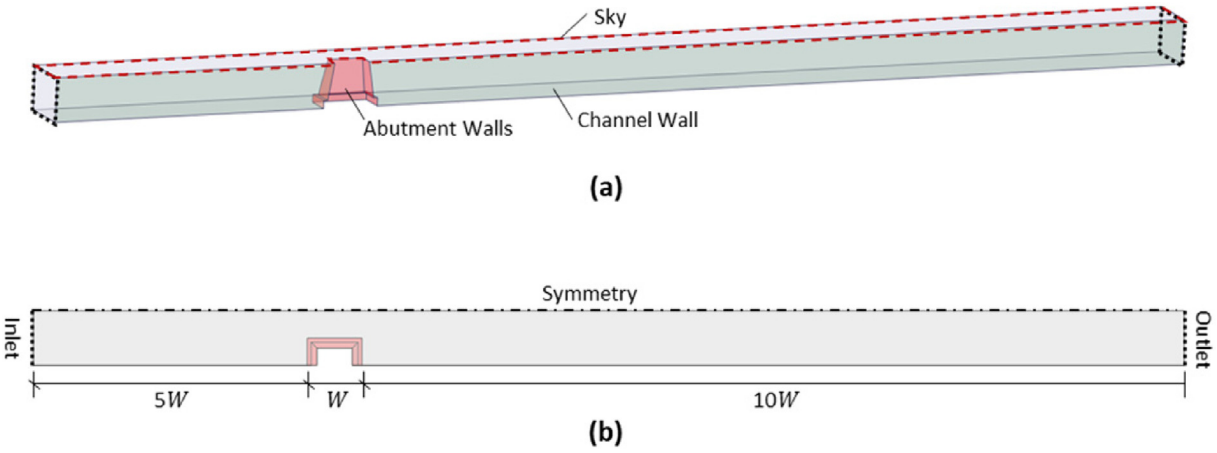

Fig. 13. (a) 3D and (b) plan view of the CFD model indicating boundary conditions.

based on its effectiveness in reproducing the experimentally measured dependence of C_D on blockage ratio, as discussed in the following.

Application of wall functions requires sufficient discretization of the near-wall region (Fig. 14c). This is quantifiable through the non-dimensional wall distance y^+ given in Eq. (13) below:

$$y^+ = \frac{\sqrt{\tau_\omega \rho} y_1}{\nu} \tag{13}$$

where τ_ω, ρ, y_1 denote the wall shear stress, the fluid density, and the distance from the centre of the first cell to the wall, respectively. To satisfy the requirement for $30 < y^+ < 300$ as per (Fluent Theory Guide, 2013), we sufficiently refined the grid, prior to every one of the CFD analyses presented in the following, to achieve minimum $y^+ > 30$ and average $y^+ \approx 100$. As a result, the size of the mesh grows with increasing Re, reaching up to 11 million cells, when $Re = 1 \times 10$ (Marchi et al., 2010).

3.2.2. Channel widening and blockage effects

The magnitude of drag and lift forces acting on the abutment depends on the extent of flow obstruction caused by its impermeable, submerged body. In their study of a benchmark problem where a rectangular cylinder is fixed in the middle of a wall-confined flow (Fig. 15a), Sharify et al. (2013) and Qi et al. (2014) demonstrate that the drag coefficient is an increasing function of the blockage ratio B/L (Fig. 15b), where B is the width of the cylinder and L is the width of the channel. By analogy, the drag experienced by an abutment (a sidewall obstruction, as shown in Fig. 15c), can be correlated with an equivalent blockage ratio BR

$$BR = \frac{B_f}{L_{/2}} \tag{14}$$

Unlike the mid-stream obstacle of Fig. 15a, a sidewall obstruction produces a non-zero average lift force, $F_L{}^y$, acting on the spanwise direction

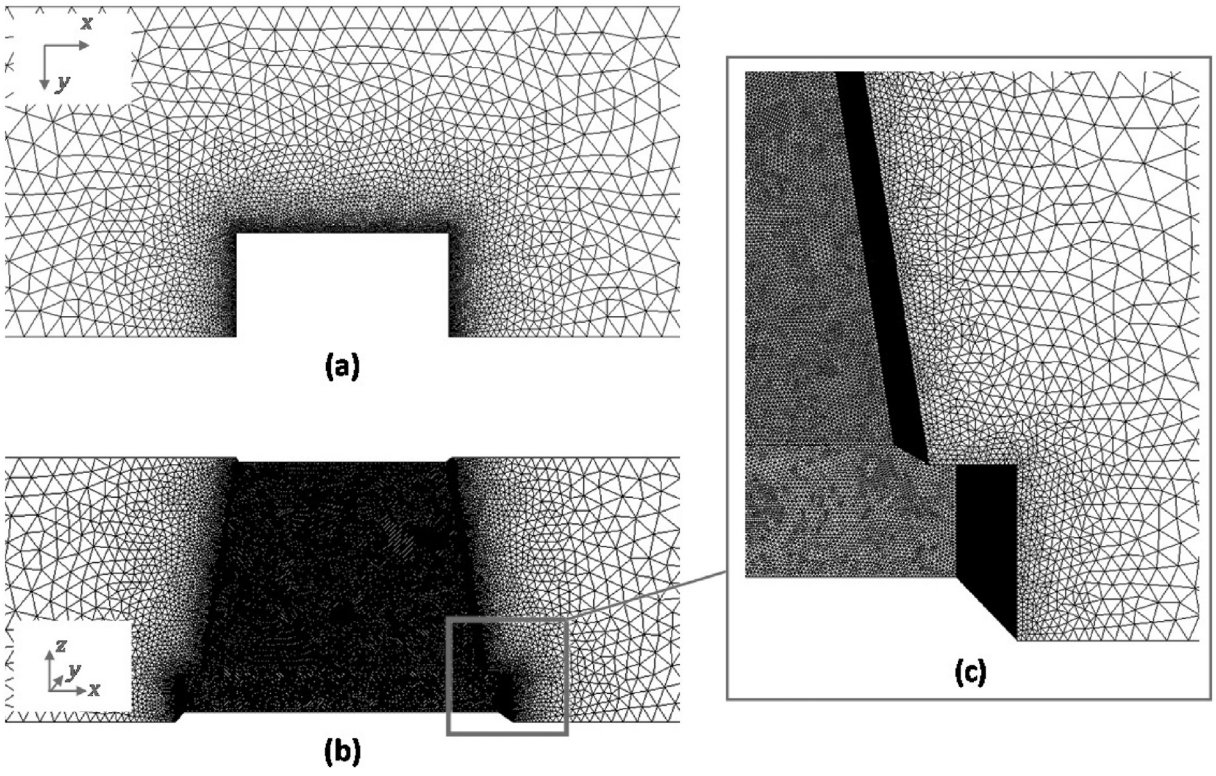

Fig. 14. (a) Plan and (b) longitudinal section snapshots of the fluid domain discretization, and (c) detail of mesh at wall boundaries.

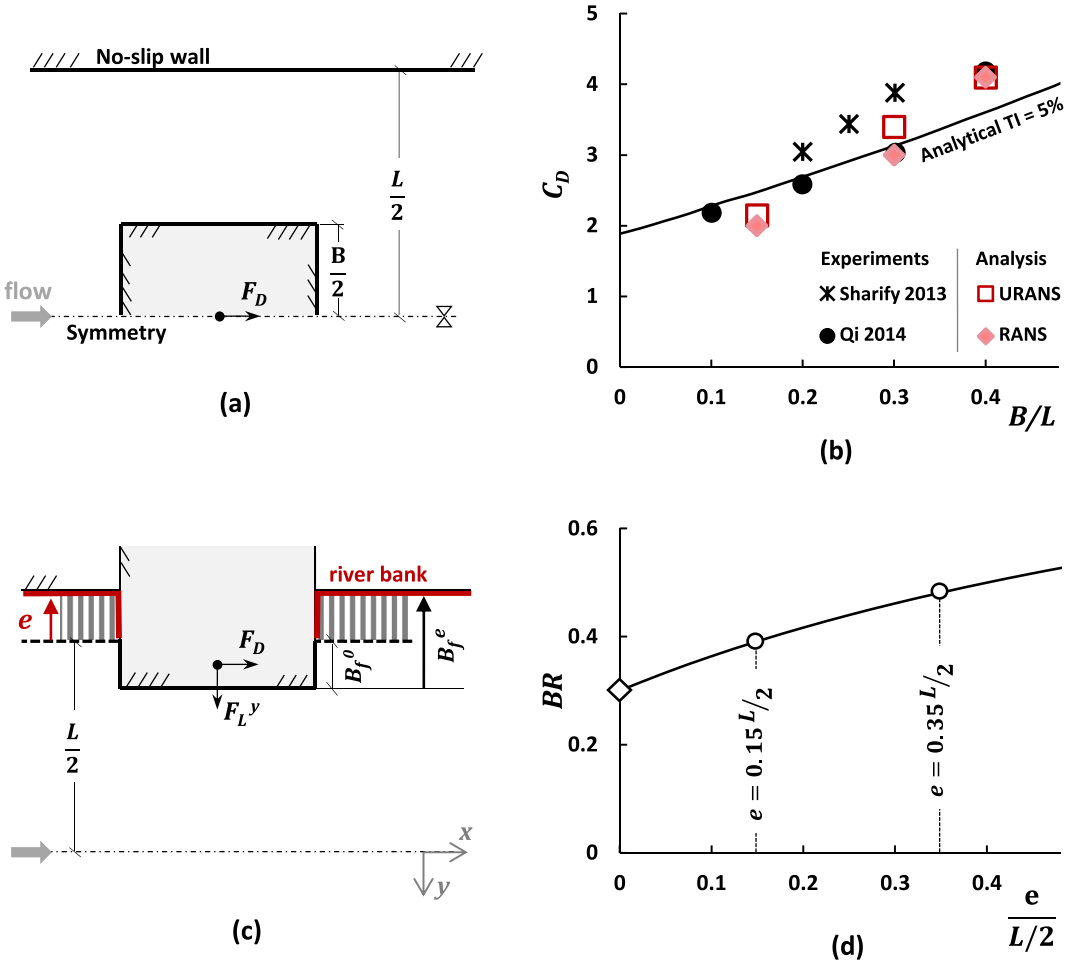

Fig. 15. Blockage effects on open channel flow: (a) the benchmark problem of a mid-stream obstacle (plan view) (b) C_D as a function of blockage ratio *BR*; (c) sidewall obstacle, i.e. abutment, where (d) *BR* is affected by lateral channel expansion *e*.

(Fig. 15c) due to the lack of symmetry. Furthermore, a non-zero lift component acts in the *z* direction ($F_L{}^z$), due to the trapezoidal shape of the abutment (i.e. variation of cross-section with depth).

Importantly, *BR* is not constant. As the abutment wing walls comprise a continuous, solid form that extends into the banks, lateral widening (*e*) of the channel results in increased blockage. In the absence of information about the original width of the riverbank upstream of Br9 and bound by the adopted simplification of a uniform rectangular channel, here we assume that $L = 20$ m, i.e. the original channel width was equal to the span of the deck. This yields an initial blockage ratio $BR^0 = 0.3$. It follows that *BR* increases with increasing *e* according to the graph of Fig. 15d. Taking into account the prominent widening of Pamissos riverbank in this event, we also consider increased levels of blockage, namely $BR = 0.4$ and $BR = 0.5$, corresponding to scenarios of lateral expansion of the channel: by 15% and 35% of the initial span, respectively. A correlation has been assumed between *e* and the scour penetration parameter *s*, such that the effective submersion width B_f^e (see Fig. 15c) is equal to *s*.

To verify that our CFD modelling methodology can reproduce the crucial dependence of C_D on *BR*, we first simulated the experimentally studied mid-stream blockage problem (Fig. 15a–b). We reproduced the geometry and flow conditions tested by Sharify et al. (2013), who consider rectangular cylinders submerged in a 4250 mm long and 200 mm wide tank with constant $Re = 1000$. Following the approach described previously regarding modelling of turbulent flow, treatment of near-wall response, and discretization, we also took advantage of the reduced size of the model to carry out both steady (RANS) and unsteady (URANS) computations. The latter was carried out according to (Catalano et al., 2003) for a total time equal to 300 B/V with a time-step of $\Delta t = 0.01\ B/V$. Both types of analysis show good agreement with the experimental results, as shown in Fig. 15b. As RANS can reasonably capture the effect of blockage on average flow characteristics, it is preferable to the computationally exhaustive URANS for the analysis of the large-scale 3D problem.

The surface velocity contour plots of Fig. 16a–c show how flow around the abutment is influenced by *BR*, and hence by *e*. As the abutment blocks a significant part of the channel area, the flow separates, at some distance ahead of it, and accelerates towards the centreline. Contraction leads to substantially amplified streamwise velocities at the bridge opening, from 1.4 *V*, when $BR = 0.3$, to as much as 2.5 *V* when $BR = 0.5$. The structure of the flow downstream of the abutment is also affected. Flow separation becomes significant, as evidenced by the zero velocity zones. A massive wake develops for $BR > 3$, extending over 3 abutment widths (*W*) downstream.

The pressure on the upstream face of the abutment rises accordingly. For an inlet velocity of $V = 0.6$ m/s and $BR = 0.3$, the computed pressure field (Fig. 16d) displays an almost linear distribution with depth, reaching a maximum of 156 kPa. Pressures become more uniform and 2–3 times higher in magnitude for $BR = 0.4$–0.5 (Fig. 16e–f). As a result, the drag coefficient (C_D) shows a strong dependence on *BR*. Table 3 lists drag and lift coefficients for the three levels of *BR*. Although our analysis considered a range of inlet velocities ($1 \times 10^6 < Re \leq 1 \times 10$ (Marchi et al., 2010)), drag and lift coefficients showed little variation with respect to *Re*, as commonly found in RANS simulations (Catalano et al., 2003; Benim et al., 2007). Lift coefficients seem unaffected by *BR*. However, this is not the

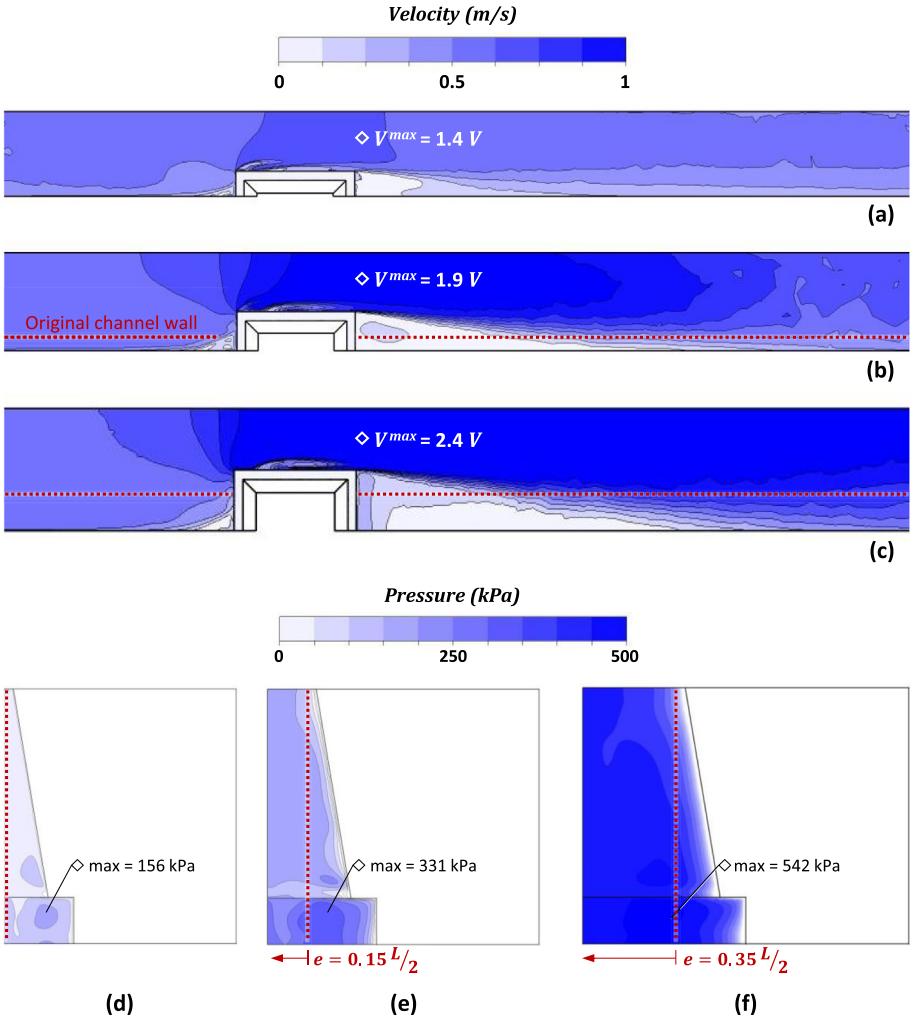

Fig. 16. Effect of increasing blockage due to lateral channel expansion on (a)–(c) streamwise flow velocities and (d) – (f) pressure at the upstream wall of the abutment, for constant inlet $V = 0.6$ m/s.

case for the respective loads which, as per the definition of the coefficients, are proportionally related to the area of the obstacle:

$$F_{D/L} = \frac{1}{2} C_{D/L} \rho V^2 A_s \tag{15}$$

where A_s is the area of the abutment that obstructs the flow.

Hence, hydrodynamic loading increases in all three directions with increasing *BR*. This is evident in Fig. 17a which plots the total force with respect to *V*. Interestingly, increasing *BR* also leads to a drastic drop of the gradient of the loading path F_L^Y/F_D (Fig. 17b), implying a tendency of the drag component to predominate over lift.

3.3. The combined effect of scouring and hydrodynamic actions

A forensic investigation of the flow conditions that led to the collapse of the western abutment of Br9 is based on the previously discussed evidence that the *BR* has a strong influence on the $F_D - F_L$ loading path (Fig. 17b).

Table 3
Abutment drag and lift coefficients.

BR	A_s (m^2)	C_D	C_L^Y	C_L^Z
0.3	16.5	0.92	4.78	1.31
0.4	35.4	2.41	5.15	1.39
0.5	61	4.53	4.97	1.26

Hence, we presume it to be reflected in the resulting deformations, i.e. in the rupture pattern. Most importantly, using the CFD-deduced correlation between loads and inlet velocity (*V*), we can estimate the minimum flow intensity required to cause the observed failure.

In our analysis, we make use of the simplified mechanical model B (Fig. 10a–b) to investigate a number of key parameters, as listed in Table 4. FE simulations include a total of four steps, static and dynamic, namely:

1. Static step: application of self-weights;
2. Static step: scour penetration (Fig. 10b);
3. Static step: buoyancy, implemented as surface pressure at the deck (= $\rho g d$) and at the exposed, i.e. wet, part of the abutment ($\rho g h$);
4. Dynamic step: Progressively increasing, monotonic hydrodynamic loads applied quasi-statically at the centre of mass of the deck and at the centre of mass of the instream part of the abutment. A set of load protocols were devised, following the F_D, F_L vs. *V* relationships produced by the CFD analysis, assuming that *V* could range from 0.1 m/s to 10 m/s (extreme lower and upper values, respectively).

Figs. 18 and 19 summarize selected results from the parametric investigation of the combined scour–flow blockage effects. The onset of failure is easily recognisable in the plots of Fig. 18a, where the spanwise displacement of the abutment δy (with reference to the mid-point of its footing) is shown as a function of *V*. As expected, scour penetration, associated with increased *BR*, reduces substantially the tolerance for high flow velocities.

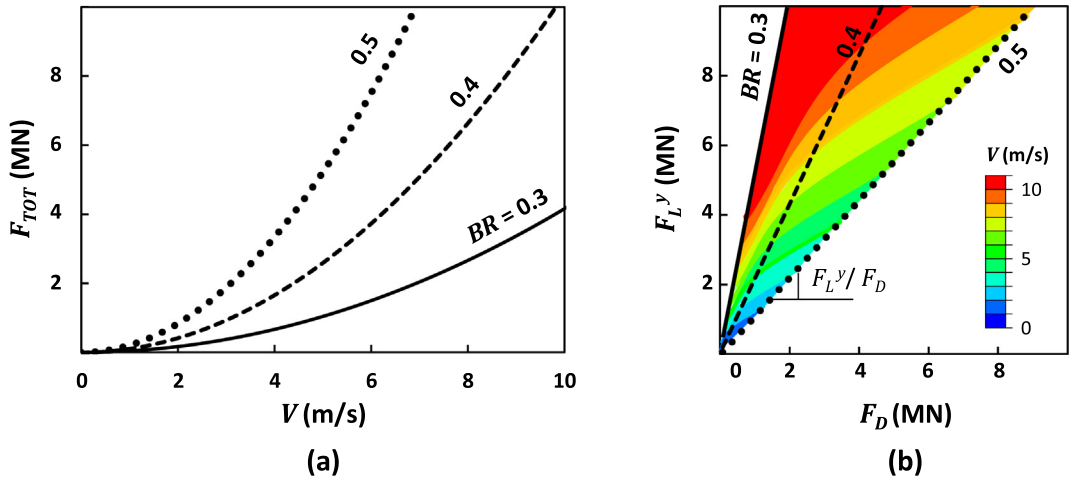

Fig. 17. Steady-state hydrodynamic loading of the abutment: (a) total force with respect to inlet velocity and (b) drag – (spanwise) lift loading paths for the different blockage ratios considered.

Table 4
Variables considered in the parametric investigation.

Parameter	Investigated values
Scour (s/Bf)	0, 1, 1.3, 1.7
Flow blockage (BR)	0, 0.3, 0.4, 0.5
Inundation (h^*)	Moderate ($0.5 > h^* \leq 1.3$), Heavy ($h^* > 1.3$)
Deck – abutment connection	Reinforced/unreinforced
Joints	With/without tension cut-off

Rather unrealistic velocity magnitudes (exceeding 16 m/s) would be required to cause failure with $BR \leq 0.3$. By contrast, higher blockage due to lateral (westward) expansion of the stream lowers the safety margin to 12 m/s and 7 m/s for $BR = 0.4$ and $BR = 0.5$, respectively.

Interestingly, the role of deck inundation (h^*) appears less significant, especially at high levels of s and BR. In fact, results from simulations with $BR = 0$ indicate that the observed failure pattern cannot be reproduced if the effect of the deck–flow interaction is considered in isolation, i.e., assuming no scour or blockage.

In the snapshots of Fig. 19, concrete damage is visualized through plastic strain contours. Planes of strain localization (implying crack propagation) are compared to the observed rupture pattern. Apart from Fig. 19a–b ($BR = 0.3$), all snapshots indicate incipient collapse of the abutment. A striking resemblance is achieved in Fig. 19e between the numerically computed failure mechanism and the actual damage. This model captures the pattern of the main rupture, developed along the wing walls (upstream U and downstream D), as well as the secondary rupture plane that was observed at the remaining part of the face (Fig. 4b) – (spanwise S). It suggests that the simulated loading combination ($s/B_f = 1.7$, $BR = 0.5$, $h^* \leq 1.3$) is a reasonable approximation of the actual conditions that caused the failure of the abutment of Br9. Importantly, this is one of the least favourable scenarios that we investigated, enabling failure for $V \approx 7$ m/s. Notably, the estimation of this critical flow velocity value is not sensitive to the assumed value of secant soil stiffness G_{sec}, as indicated in Fig. 18b.

The estimated critical flow velocity can be used as input in 1-D or 2-D hydraulic models of the Pamissos catchment for further analysis of the impact of this flood and re-assessment of flood vulnerability for infrastructure in the river environment.

4. Concluding remarks

The paper has documented a novel approach to the characterization of flood intensity based on field evidence and numerical modelling of a structural failure. This can be particularly useful for the analysis of extreme

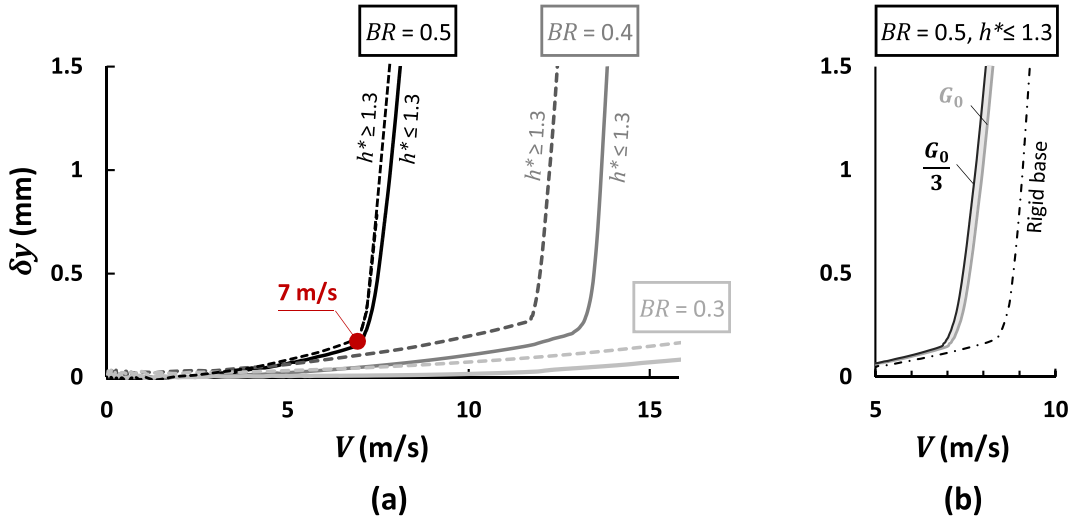

Fig. 18. Spanwise horizontal displacements computed at the mid-point of the collapsed footing with respect to inlet flow velocity for (a) all the investigated scenarios of combined scour – deck inundation – lateral flow constrictions scenarios, and (b) various assumptions for the secant soil stiffness $G_{sec}/G_0 = 0.33$–1.

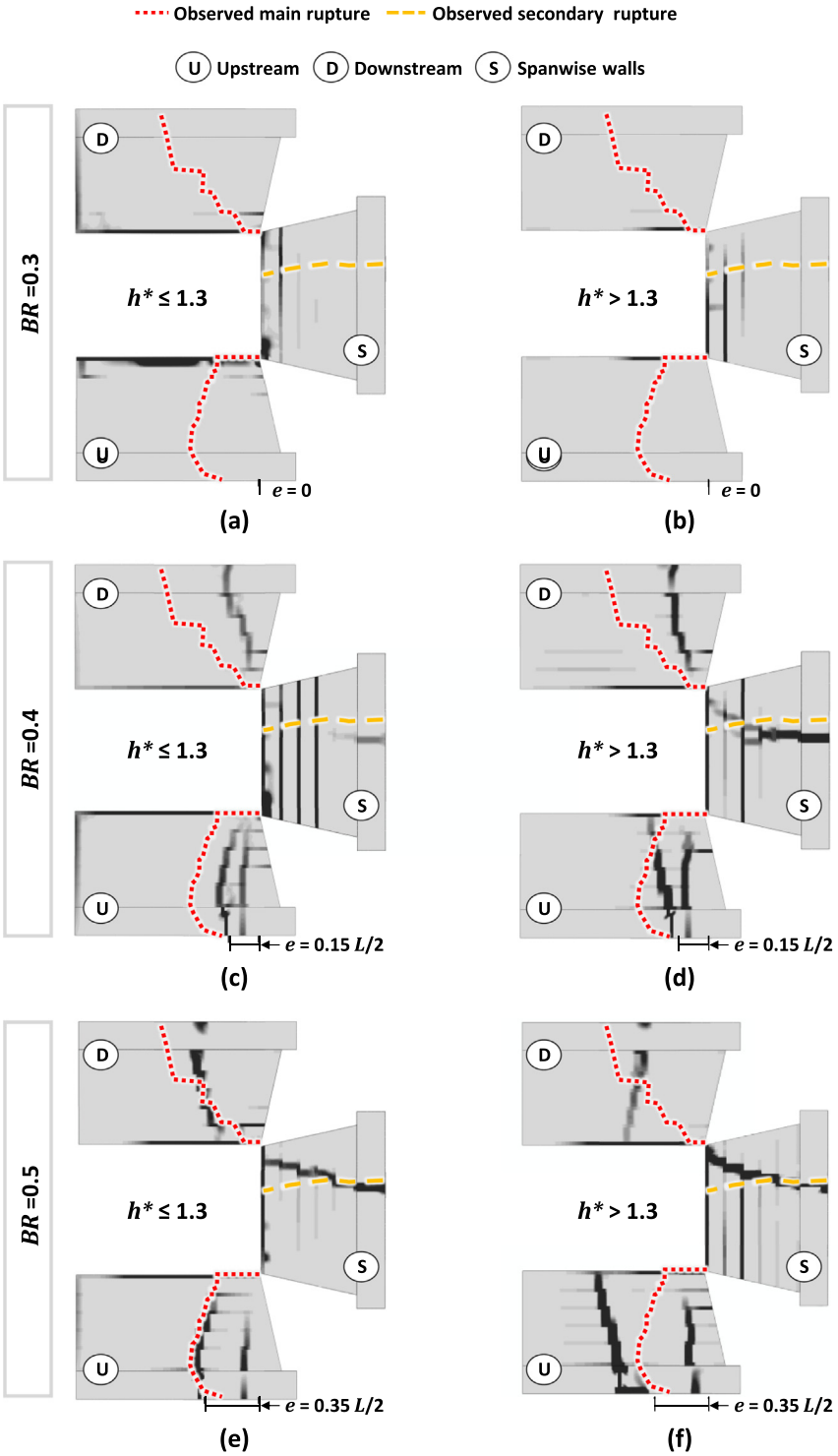

Fig. 19. Comparison of observed rupture pattern with predicted plastic strain localizations for: (a) $V = 16$ m/s, $BR = 0.3$, $h^* \leq 1.3$; (b) $V = 16$ m/s, $BR = 0.3$, $h^* > 1.3$; (c) $V = 14$ m/s, $BR = 0.4$, $h^* \leq 1.3$; (d) $V = 13$ m/s, $BR = 0.3$, $h^* > 1.3$; (e) $V = 8$ m/s, $BR = 0.5$, $h^* \leq 1.3$; (f) $V = 8$ m/s, $BR = 0.5$, $h^* > 1.3$.

flood events occurring in ungauged watersheds, especially in view of the prospected climate-exacerbated floods which, like the very recent ones in Germany, can cause disruption and damage to the built environment. Incorporating the effect of hydrodynamic loads, in addition to scouring, the methodology captures failure mechanisms that are controlled by flow–structure interaction. Such mechanisms may be prevailing in high velocity flows, as is the case in flash floods.

Insights on the role of scour penetration and flow blockage are discussed in detail to enhance understanding of riverine bridge vulnerability and highlight the need to incorporate such dynamic parameters in the assessment of risk. As flash floods often cause bank erosion and lateral expansion of the channel, assessment of asset risk and resilience should consider the potential of increased blockage ratios occurring when bridges are supported by continuous solid structures.

The Structure-from-Motion method was used to produce a high-fidelity 3D model of the case-study bridge based on UAV enabled imagery using survey-grade GCPs and CPs. The geometry was reproduced numerically in mechanical and CFD analyses to resolve several engineering disputes

regarding the failure mechanism and the safety of the new bridge constructed on top (mitigation solution). More specifically, the analysis indicates that:

1. Despite the lack of reinforcement, the concrete wingwalls of the abutment can safely sustain the weight of the structure, even when they are exposed by a large scour hole. Scour, alone, could not have caused this catastrophic failure, had it not been combined with hydrodynamic loads of sufficient magnitude. This finding led to the need for a CFD analysis.
2. Failure of the abutment occurs when the mean flow velocity upstream exceeds 7 m/s. We believe this to be a lower bound estimate of the intensity of this flood.
3. The eastern (currently standing) abutment did not fail thanks to its intact foundation. We suggest that it can safely survive a similar flood, as long as it is not compromised by scour.
4. The remaining parts of the failed abutment (characterized as sections of questionable stability) are reinforced with steel rebars, unlike the wingwalls. As such, they can safely carry the dead weight of the old deck (which has not been demolished) and they are unlikely to compromise the safety of the new bridge.

5. Limitations

Several assumptions have been the basis of our numerical method, as discussed throughout the text. Moreover, the reader should bear in mind that the presented study has not accounted for the following, potentially important, factors:

- High concentration of sediments in the flow (mudflow).
- Additional actions due to debris accumulation or impact forces due to floating debris.
- The curved shape of the river (meander), which is the reason why the scour hole developed only on the western support of the bridge.
- The effect of the presence of the deck on the hydrodynamic loads imposed on the abutment, and vice-versa, i.e., abutment–deck interaction, has not been considered as this would require CFD modelling of the entire bridge.

CRediT authorship contribution statement

Marianna Loli: Conceptualization, Methodology, Field Investigation, Numerical analysis, Data curation, Visualization, Writing original draft, Reviewing and Editing. **Stergios Aristoteles Mitoulis**: Conceptualization, Resources, Reviewing and Editing. **Angelos Tsatsis**: Numerical analysis, Resources, Reviewing and Editing. **John Manousakis**: Field Investigation, UAV mapping, Data curation. **Rallis Kourkoulis**: Conceptualization, Field Investigation, Reviewing and Editing. **Dimitrios Zekkos**: UAV mapping, Data curation, Reviewing and Editing.

Declaration of competing interest

The authors declare that they have no known competing financial interests or personal relationships that could have appeared to influence the work reported in this paper.

Acknowledgements

This study has been funded by the European Union H2020-Marie Skłodowska-Curie Research Grants Scheme MSCA-IF-2019 (grant agreement No 895432: ReBounce-Integrated resilience assessment of bridges and transport networks exposed to hydraulic hazards). The numerical work was carried out at the University of Surrey without interruptions, although the university was under lockdown because of the COVID-19 pandemic, thanks to the university's staff and particularly thanks to valuable support from Dr. Matthew Oldfield.

The authors are grateful for the testimonies and the abundance of information shared by the people of Mouzaki and Ellinokastro. In particular, we wish to thank: Mr. Konstantinos Pistrikas, hydraulic engineer from the city of Karditsa for his valuable directions, especially on the first days of our surveys; Mr. Nikos Kourtis (local civil engineering consultant) for access to historical information and documentation of recent inspection findings; and Ms. Vaso Petsia (Karditsa council services) for her input regarding the reconstruction efforts and for providing access to design information and reports from past investigations.

Appendix A. Supplementary data

Supplementary data to this article can be found online at https://doi.org/10.1016/j.scitotenv.2022.153661.

References

Afzal, M.S., Bihs, H., Kumar, L., 2020. Computational fluid dynamics modeling of abutment scour under steady current using the level set method. Int. J. Sediment Res. 35 (4), 355–364. https://doi.org/10.1016/j.ijsrc.2020.03.003.

Agalianos, A., Sieber, M., Anastasopoulos, I., 2020. Cost-effective analysis technique for the design of bridges against strike-slip faulting. Earthq. Eng. Struct. Dyn. 49 (11), 1137–1157. https://doi.org/10.1002/eqe.3282.

Ahamed, T., Duan, J.G., Jo, H., 2020. Flood-fragility analysis of instream bridges–consideration of flow hydraulics, geotechnical uncertainties, and variable scour depth. Struct. Infrastruct. Eng., 1–14 https://doi.org/10.1080/15732479.2020.1815226.

Alabbad, Y., Mount, J., Campbell, A.M., Demir, I., 2021. Assessment of transportation system disruption and accessibility to critical amenities during flooding: Iowa case study. Sci. Total Environ. 793, 148476. https://doi.org/10.1016/j.scitotenv.2021.148476 Nov.

Alfarah, B., López-Almansa, F., Oller, S., 2017. New methodology for calculating damage variables evolution in plastic damage model for RC structures. Eng. Struct. 132, 70–86. https://doi.org/10.1016/j.engstruct.2016.11.022.

Antoniou, M., Nikitas, N., Anastasopoulos, I., Fuentes, R., 2020. Scaling laws for shaking table testing of reinforced concrete tunnels accounting for post-cracking lining response. Tunn. Undergr. Sp. Technol. 101 (May), 103353. https://doi.org/10.1016/j.tust.2020.103353.

Argyroudis, S.A., Mitoulis, S.A., 2021. Vulnerability of bridges to individual and multiple hazards- floods and earthquakes. Reliab. Eng. Syst. Saf. 210 (March), 107564. https://doi.org/10.1016/j.ress.2021.107564.

Argyroudis, S.A., Mitoulis, S.A., Hofer, L., Zanini, M.A., Tubaldi, E., Frangopol, D.M., 2020. Resilience assessment framework for critical infrastructure in a multi-hazard environment: case study on transport assets. Sci. Total Environ. 714, 1–49. https://doi.org/10.1016/j.scitotenv.2020.136854.

Bažant, Z.P., Oh, B.H., 1983. Crack band theory for fracture of concrete. Matériaux Constr. 16 (3), 155–177. https://doi.org/10.1007/BF02486267 May.

Behnam, H., Kuang, J.S., Samali, B., 2018. Parametric finite element analysis of RC wide beam-column connections. Comput. Struct. 205, 28–44. https://doi.org/10.1016/j.compstruc.2018.04.004.

Benim, A.C., Cagan, M., Nahavandi, A., Pasaqualotto, E., 2007. RANS predictions of turbulent flow past a circular cylinder over the critical regime. Proc. 5th IASME/WSEAS Int. Conf. Fluid Mech. Aerodyn, pp. 232–237.

Bolourian, N., Hammad, A., 2020. LiDAR-equipped UAV path planning considering potential locations of defects for bridge inspection. Autom. Constr. 117, 103250. https://doi.org/10.1016/j.autcon.2020.103250 Sep.

Bray, J.D., Frost, J.D., Rathje, E.M., Garcia, F.E., 2019. Recent advances in geotechnical post-earthquake reconnaissance. Front. Built Environ. 5. https://doi.org/10.3389/fbuil.2019.00005 Jan.

C. for E. and H. (CEH), 1999. Flood Estimation Handbook.

Catalano, P., Wang, M., Iaccarino, G., Moin, P., 2003. Numerical simulation of the flow around a circular cylinder at high Reynolds numbers. Int. J. Heat Fluid Flow 24 (4), 463–469. https://doi.org/10.1016/S0142-727X(03)00061-4.

CEB-FIP, 2010. Model Code 2010. Thomas Tel., London.

Centre, C.-C.M., 2019. EN 13791 - Assessment of In-situ Compressive Strength in Structures and Precast Concrete Components.

Chan, B., Guan, H., Jo, J., Blumenstein, M., 2015. Towards UAV-based bridge inspection systems: a review and an application perspective. Struct. Monit. Maint. 2 (3), 283–300. https://doi.org/10.12989/smm.2015.2.3.283 Sep.

Chen, Q., Wang, L., Zhao, H., 2009. Hydrodynamic investigation of coastal bridge collapse during hurricane Katrina. J. Hydraul. Eng. 135 (3), 175–186. https://doi.org/10.1061/(asce)0733-9429(2009)135:3(175).

Chen, S., Laefer, D.F., Mangina, E., Zolanvari, S.M.I., Byrne, J., 2019. UAV bridge inspection through evaluated 3D reconstructions. J. Bridg. Eng. 24 (4), 05019001. https://doi.org/10.1061/(ASCE)BE.1943-5592.0001343 Apr.

Chrisohoides, A., Sotiropoulos, F., Sturm, T.W., 2003. Coherent structures in flat-bed abutment flow: computational fluid dynamics simulations and experiments. J. Hydraul. Eng. 129 (3), 177–186. https://doi.org/10.1061/(ASCE)0733-9429(2003)129:3(177) Mar.

Ciancimino, A., 2021. Performance of Caisson Foundations Subjected to Flood-induced Scour. Politecnico di Torino.

S. F. Andrea Ciancimino, Liam Jones, Lampros Sakellariadis, Ioannis Anastasopoulos, n.d. "Geotechnique experimental assessment of the performance of a bridge pier subjected to flood- induced scour," *Under Rev.*

Clark, L.A., Gill, B.S., 1985. Shear strength of smooth unreinforced construction joints. Mag. Concr. Res. 37 (131), 95–100. https://doi.org/10.1680/macr.1985.37.131.95.
Cornwall, W., 2021. Europe's deadly floods leave scientists stunned. Science 373 (6553), 372–373. https://doi.org/10.1126/science.373.6553.372 Jul.
Fluent Theory Guide, 2013. Ansys Fluent Theory Guide. vol. 15317, no. November. ANSYS Inc., USA, pp. 724–746 Sep http://scholar.google.com/scholar?hl=en&btnG=Search&q=intitle:ANSYS+FLUENT+Theory+Guide#0.
Gaume, E., et al., 2009. A compilation of data on european flash floods. J. Hydrol. 367 (1–2), 70–78. https://doi.org/10.1016/j.jhydrol.2008.12.028.
Gazetas, G., 1983. Analysis of machine foundation vibrations: state of the art. Int. J. Soil Dyn. Earthq. Eng. 2 (1), 2–42. https://doi.org/10.1016/0261-7277(83)90025-6 Jan.
González-Alemán, J.J., Pascale, S., Gutierrez-Fernandez, J., Murakami, H., Gaertner, M.A., Vecchi, G.A., 2019. Potential increase in hazard from Mediterranean hurricane activity with global warming. Geophys. Res. Lett. 46 (3), 1754–1764. https://doi.org/10.1029/2018GL081253.
Greco, F., Lonetti, P., Nevone Blasi, P., 2020. Vulnerability analysis of bridge superstructures under extreme fluid actions. J. Fluids Struct. 93, 102843. https://doi.org/10.1016/j.jfluidstructs.2019.102843.
Greenwood, W.W., Lynch, J.P., Zekkos, D., 2019. Applications of UAVs in civil infrastructure. J. Infrastruct. Syst. 25 (2), 04019002. https://doi.org/10.1061/(ASCE)IS.1943-555X.0000464 Jun.
Ho, D.-T., Grøtli, E.I., Sujit, P.B., Johansen, T.A., Sousa, J.B., 2015. Optimization of wireless sensor network and UAV data acquisition. J. Intell. Robot. Syst. 78 (1), 159–179. https://doi.org/10.1007/s10846-015-0175-5 Apr.
Jawhar, I., Mohamed, N., Al-Jaroodi, J., Zhang, S., 2014. A framework for using unmanned aerial vehicles for data collection in linear wireless sensor networks. J. Intell. Robot. Syst. 74 (1–2), 437–453. https://doi.org/10.1007/s10846-013-9965-9 Apr.
Jempson, M.A., 2000. Flood and Debris Loads on Bridges.
Jongman, B., et al., 2014. Increasing stress on disaster-risk finance due to large floods. Nat. Clim. Chang. 4 (4), 264–268. https://doi.org/10.1038/nclimate2124 Apr.
Kara, S., Kara, M.C., Stoesser, T., Sturm, T.W., 2015. Free-surface versus rigid-lid LES computations for bridge-abutment flow. J. Hydraul. Eng. 141 (9), 04015019. https://doi.org/10.1061/(asce)hy.1943-7900.0001028.
Kendon, E.J., Roberts, N.M., Fowler, H.J., Roberts, M.J., Chan, S.C., Senior, C.A., 2014. Heavier summer downpours with climate change revealed by weather forecast resolution model. Nat. Clim. Chang. 4 (7), 570–576. https://doi.org/10.1038/nclimate2258 Jul.
Kerenyi, K., Sofu, T., Guo, J., 2009. [Online]. Available:Hydrodynamic Forces on Inundated Bridge Decks , p. 48. http://www.fhwa.dot.gov/publications/research/infrastructure/hydraulics/09028/.
Krahl, P.A., Carrazedo, R., El Debs, M.K., 2018. Mechanical damage evolution in UHPFRC: experimental and numerical investigation. Eng. Struct. https://doi.org/10.1016/j.engstruct.2018.05.064.
Kundzewicz, Z.W., et al., 2014. Flood risk and climate change: global and regional perspectives. Hydrol. Sci. J. 59 (1), 1–28. https://doi.org/10.1080/02626667.2013.857411 Jan.
Launder, B.E., Spalding, D.B., 1983. THE NUMERICAL COMPUTATION OF TURBULENT FLOWS. Numerical Prediction of Flow, Heat Transfer, Turbulence and Combustion. vol. 3. Elsevier, pp. 96–116.
Lee, J., Fenves, G.L., 1998. Plastic-damage model for cyclic loading of concrete structures. J. Eng. Mech. 124 (8), 892–900. https://doi.org/10.1061/(asce)0733-9399(1998)124:8(892).
Lei, B., Wang, N., Xu, P., Song, G., 2018. New crack detection method for bridge inspection using UAV incorporating image processing. J. Aerosp. Eng. 31 (5), 04018058. https://doi.org/10.1061/(ASCE)AS.1943-5525.0000879 Sep.
Llasat, M.C., et al., 2010. High-impact floods and flash floods in Mediterranean countries: the FLASH preliminary database. Adv. Geosci. 23, 47–55. https://doi.org/10.5194/adgeo-23-47-2010.
Lubliner, J., Oliver, J., Oller, S., Oñate, E., 1989. A plastic-damage model for concrete. Int. J. Solids Struct. 25 (3), 299–326. https://doi.org/10.1016/0020-7683(89)90050-4 Jan.
Malavasi, S., Guadagnini, A., 2003. Hydrodynamic loading on river bridges. J. Hydraul. Eng. 129 (11), 854–861. https://doi.org/10.1061/(asce)0733-9429(2003)129:11(854).
Malavasi, S., Guadagnini, A., 2007. Interactions between a rectangular cylinder and a free-surface flow. J. Fluids Struct. 23 (8), 1137–1148. https://doi.org/10.1016/j.jfluidstructs.2007.04.002.
Marchi, L., Borga, M., Preciso, E., Gaume, E., 2010. Characterisation of selected extreme flash floods in Europe and implications for flood risk management. J. Hydrol. 394 (1–2), 118–133. https://doi.org/10.1016/j.jhydrol.2010.07.017.
Melville, B.W., 1992. Local scour at bridge abutments. J. Hydraul. Eng. 118 (4), 615–631. https://doi.org/10.1061/(ASCE)0733-9429(1992)118:4(615) Apr.
Melville, B.W., 1997. Pier and abutment scour: integrated approach. J. Hydraul. Eng. 123 (2), 125–136. https://doi.org/10.1061/(asce)0733-9429(1997)123:2(125).
Mitoulis, S.A., Argyroudis, S.A., Loli, M., Imam, B., 2021. Restoration models for quantifying flood resilience of bridges. Eng. Struct. 238, 112180. https://doi.org/10.1016/j.engstruct.2021.112180 Jul.
Nishar, A., Richards, S., Breen, D., Robertson, J., Breen, B., 2016. Thermal infrared imaging of geothermal environments and by an unmanned aerial vehicle (UAV): a case study of the Wairakei – Tauhara geothermal field, Taupo, New Zealand. Renew. Energy 86, 1256–1264. https://doi.org/10.1016/j.renene.2015.09.042 Feb.
Oliveto, G., Hager, W.H., 2002. Temporal evolution of clear-water pier and abutment scour. J. Hydraul. Eng. 128 (9), 811–820. https://doi.org/10.1061/(ASCE)0733-9429(2002)128:9(811) Sep.
Oudenbroek, K., et al., 2018. Hydrodynamic and debris-damming failure of bridge decks and piers in steady flow. Geosci. 8 (11). https://doi.org/10.3390/geosciences8110409.
Qi, Z.X., Eames, I., Johnson, E.R., 2014. Force acting on a square cylinder fixed in a free-surface channel flow. J. Fluid Mech. 756, 716–727. https://doi.org/10.1017/jfm.2014.455.
Rossi, M., Brunelli, D., 2016. Autonomous gas detection and mapping with unmanned aerial vehicles. IEEE Trans. Instrum. Meas. 65 (4), 765–775. https://doi.org/10.1109/TIM.2015.2506319 Apr.
Scozzese, F., Ragni, L., Tubaldi, E., Gara, F., 2019. Modal properties variation and collapse assessment of masonry arch bridges under scour action. Eng. Struct. 199 (September), 109665. https://doi.org/10.1016/j.engstruct.2019.109665.
Sharify, A.N.E.M., Saito, H., Harasawa, H., Takahasi, S., 2013. Experimental and Numerical Study of Blockage Effects on Flow Characteristics around Square-Section Cylinder. vol. 13, pp. 85–91.
Shih, T.-H., Liou, W.W., Shabbir, A., Yang, Z., Zhu, J., 1995. A new k-□ eddy viscosity model for high Reynolds number turbulent flows. Comput. Fluids 24 (3), 227–238. https://doi.org/10.1016/0045-7930(94)00032-T Mar.
SIMULIA, 2014. Abaqus Documentation (6.14). Dassault Systèmes Simulia Corp., Providence, RI, USA.
Snavely, N., Seitz, S.M., Szeliski, R., 2008. Modeling the world from internet photo collections. Int. J. Comput. Vis. 80 (2), 189–210. https://doi.org/10.1007/s11263-007-0107-3 Nov.
Sturm, T.W., Janjua, N.S., 1994. Clear-water scour around abutments in floodplains. J. Hydraul. Eng. 120 (8), 956–972. https://doi.org/10.1061/(ASCE)0733-9429(1994)120:8(956) Aug.
Teng, G.E., et al., 2017. MINI-UAV LIDAR FOR POWER LINE INSPECTION. Int. Arch. Photogramm. Remote Sens. Spat. Inf. Sci. XLII-2/W7, 297–300. https://doi.org/10.5194/isprs-archives-XLII-2-W7-297-2017 Sep.
Teruzzi, A., Ballio, F., Armenio, V., 2009. Turbulent stresses at the bottom surface near an abutment: laboratory-scale numerical experiment. J. Hydraul. Eng. 135 (2), 106–117. https://doi.org/10.1061/(asce)0733-9429(2009)135:2(106).
Tito, J.C.Solís, 2019. EVALUATION OF SHEAR STRENGTH PARAMETERS OF GRAVEL SOILS WITH DIFFERENT SHAPE AND RELATIVE DENSITY. Int. J. GEOMATE 16 (54). https://doi.org/10.21660/2019.54.8231 Feb.
Tous, M., Zappa, G., Romero, R., Shaffrey, L., Vidale, P.L., 2016. Projected changes in medicanes in the HadGEM3 N512 high-resolution global climate model. Clim. Dyn. 47 (5–6), 1913–1924. https://doi.org/10.1007/s00382-015-2941-2.
Tubaldi, E., Macorini, L., Izzuddin, B.A., 2018. Three-dimensional mesoscale modelling of multi-span masonry arch bridges subjected to scour. Eng. Struct. 165 (June 2017), 486–500. https://doi.org/10.1016/j.engstruct.2018.03.031.
Vui Chua, K., Fraga, B., Stoesser, T., Ho Hong, S., Sturm, T., 2019. Effect of bridge abutment length on turbulence structure and flow through the opening. J. Hydraul. Eng. 145 (6), 04019024. https://doi.org/10.1061/(asce)hy.1943-7900.0001591.
Wartman, J., et al., 2020. Research needs, challenges, and strategic approaches for natural hazards and disaster reconnaissance. Front. Built Environ. 6. https://doi.org/10.3389/fbuil.2020.573068 Nov.
Yorozuya, A., Ettema, R., 2015. Three abutment scour conditions at bridge waterways. J. Hydraul. Eng. 141 (12), 04015028. https://doi.org/10.1061/(asce)hy.1943-7900.0001053.
Zekkos, D., Zalachoris, G., 2020. The September 18-20 2020 Medicane Ianos Impact on Greece Phase I Reconnaissance Report Geotechnical Extreme Events Reconnaissance Association. https://doi.org/10.18118/G6MT1.
Zekkos, J.L., Manousakis, D.J., Greenwood, W., 2016. Immediate UAV-enabled Infrastructure Reconnaissance Following Recent Natural Disasters: Case Histories From Greece.
Zekkos, C., Greenwood, D., Manousakis, W., Athanasopoulos-Zekkos, J., Clark, A., Cook, M., Saroglou, K.L., 2018. Lessons learned from the application of UAV-enabled structure-from-motion photogrammetry in geotechnical engineering. Int. J. Geoengin. Case Hist. 4 (4), 254–274. https://doi.org/10.4417/IJGCH-04-04-03.
Zhang, L., Wang, P., Yang, W., Zuo, W., Gu, X., Yang, X., 2018. Geometric characteristics of spur dike scour under clear-water scour conditions. Water (Switzerland) 10 (6). https://doi.org/10.3390/w10060680.
Zhang, C., Zhang, X., Huang, M., Tang, H., 2019. Responses of caisson-piles foundations to long-term cyclic lateral load and scouring. Soil Dyn. Earthq. Eng. 119, 62–74. https://doi.org/10.1016/j.soildyn.2018.12.026 Apr.
Zischg, A.P., et al., 2018. Flood risk (d)evolution: disentangling key drivers of flood risk change with a retro-model experiment. Sci. Total Environ. 639, 195–207. https://doi.org/10.1016/j.scitotenv.2018.05.056 Oct.